



Delft University of Technology

## Advances in delamination modeling of metal/polymer systems

### Atomistic aspects

Van Der Sluis, Olaf; Iwamoto, Nancy; Qu, Jianmin; Yang, Shaorui; Yuan, Cadmus; Van Driel, Willem D.; Zhang, G. Q.

**DOI**

[10.1007/978-3-319-90362-0\\_4](https://doi.org/10.1007/978-3-319-90362-0_4)

**Publication date**

2018

**Document Version**

Final published version

**Published in**

Nanopackaging

**Citation (APA)**

Van Der Sluis, O., Iwamoto, N., Qu, J., Yang, S., Yuan, C., Van Driel, W. D., & Zhang, G. Q. (2018). Advances in delamination modeling of metal/polymer systems: Atomistic aspects. In *Nanopackaging: Nanotechnologies and Electronics Packaging, Second Edition* (pp. 129-183). Springer.  
[https://doi.org/10.1007/978-3-319-90362-0\\_4](https://doi.org/10.1007/978-3-319-90362-0_4)

**Important note**

To cite this publication, please use the final published version (if applicable).  
Please check the document version above.

**Copyright**

Other than for strictly personal use, it is not permitted to download, forward or distribute the text or part of it, without the consent of the author(s) and/or copyright holder(s), unless the work is under an open content license such as Creative Commons.

**Takedown policy**

Please contact us and provide details if you believe this document breaches copyrights.  
We will remove access to the work immediately and investigate your claim.

***Green Open Access added to TU Delft Institutional Repository***

***'You share, we take care!' - Taverne project***

***<https://www.openaccess.nl/en/you-share-we-take-care>***

Otherwise as indicated in the copyright section: the publisher is the copyright holder of this work and the author uses the Dutch legislation to make this work public.

# Chapter 4

## Advances in Delamination Modeling of Metal/Polymer Systems: Atomistic Aspects



Olaf van der Sluis, Nancy Iwamoto, Jianmin Qu, Shaorui Yang,  
Cadmus Yuan, Willem D. van Driel, and G. Q. Zhang

### 4.1 Introduction

The preceding chapter explains the importance of the capability to truly predict adhesion properties and delamination mechanisms in micro- and nano-electronic devices, with a particular focus on the continuum mechanical aspects relevant for metal/polymer interfaces. This chapter elaborates on the pertinent atomistic aspects for metal/polymer interfaces.

---

O. van der Sluis (✉)

Philips Research Laboratories, Eindhoven, The Netherlands

Eindhoven University of Technology, Eindhoven, The Netherlands

e-mail: [olaf.van.der.sluis@philips.com](mailto:olaf.van.der.sluis@philips.com); [o.v.d.sluis@tue.nl](mailto:o.v.d.sluis@tue.nl)

N. Iwamoto

Honeywell Performance Materials and Technologies, Sunnyvale, CA, USA

J. Qu

Tufts University, Medford, MA, USA

S. Yang

Apple, Inc., Cupertino, CA, USA

C. Yuan

Delft University of Technology, Delft, The Netherlands

Ichijouriki LS R&D, Kaohsiung City, Taiwan

W. D. van Driel

Delft University of Technology, Delft, The Netherlands

Philips Lighting, Eindhoven, The Netherlands

G. Q. Zhang

Delft University of Technology, Delft, The Netherlands

### 4.1.1 Atomistic Modeling

Molecular modeling has historically concentrated on chemistry and either the prediction of gas phase chemical properties or bulk physical properties. As a result there was little interest in its use in materials engineering. However, over the last several decades (and particularly over the last decade), molecular modeling has gained reputation investigating material performance issues using simulation methods based upon classical mechanics. By providing path-dependent evolution of molecular interactions in order to predict specific effects of a material in its application, it has been found to be a very reliable and flexible platform from which to study compositional connections to performance. Molecular modeling has been especially useful for electronic materials where interfacial interactions have become increasingly important as feature sizes shrink [1–3]. As argued in the preceding chapter, it is the molecular-scale understanding that forms the basis from which to identify underlying weaknesses within a specific material or material formulation and serves as a companion to traditional engineering models such as finite element methods. The downside of molecular modeling is often the small scale of the model. This means that macroscale representation of specific interactions (or molecular combinations) under investigation are not practically possible because the calculations can scale dramatically with the system size (i.e., the number of atoms involved in the model) and become computationally unwieldy. This also means that to critically understand the nature of the material under investigation, strategies for limiting the model size are needed in order to identify the most important interactions.

Fortunately, there are years of structure-property correlations that can be drawn upon within synthetic and organic chemistry in order to weed out the critical interactions for first consideration. For instance, does the material have hydrogen bonding? Is it highly dipolar or ionic in nature? Is there large aliphatic content? And for polymers: how cross-linked is it, are there crystalline or ordered regions? Each of these questions brings with it decisions on how to build and analyze the model. Interestingly, these are common themes when looking at the molecular structure, so the question of what to model sometimes is a relatively simple one of modeling the strongest interactions against the weakest. Other times the question of what to model takes a step up in complexity which includes architectural effects and effects from multifunctional content. Adding additional variables such as the type of order along the polymer backbone (including random, blocked, and stereochemical content), the architecture of the backbone, and cross-linking can increase the model difficulty but become interesting pieces of the puzzle.

Just as interesting as the architecture, there are also common themes in simulating the structural responses with the molecular-scale perspective, such as cycling issues (thermal and/or mechanical), static or equilibrium comparisons, chemical changes, and of course the combinations. While this may seem straightforward to other modeling disciplines, to the molecular modeler it should not be, as the complexity

of the model can depend greatly upon the number of different compositional elements. Grouping and simplifying the model (or models) is a major aspect of molecular modeling. One way in which informed grouping of the chemical component has been shown to be invaluable is for the prediction of bulk properties. This has been the topic of many group-based and descriptor analysis methods, such as Jozef Bicerano's program Synthia [4] (available through Biovia), Codessa (Alan R. Katritzky, Mati Karelson, Ruslan Petrukhin, distributed by Semichem), and Cosmotherm (from Andreas Klamt distributed by Cosmologic).

### 4.1.2 Molecular Simulation Strategies

There are generally two ways to perform a typical molecular simulation: direct quantum methods or classical force field-based molecular mechanics/dynamics (including Monte Carlo methods). Quantum mechanics is the most time and computer-resource intensive model but often needed to understand the basic chemistry. It is also used when the classical force field method is not suitable for the material or property under investigation because of lack of a good representative force field. Today the most popular quantum method is density functional theory (DFT) which basically makes use of spatially dependent electron densities [5] rather than explicit Hartree-Fock calculations of the wave function or semiempirical calculations which are more approximated methods. DFT has been proven invaluable in determining most likely chemical structures, especially if formulation ingredients are the only initial known variables. DFT has also been used to modify force field-assigned atomic charges and bonding when new structures that are not necessarily known are being investigated. For instance the correct charges for ionic species can be very important to define correctly. In addition, DFT is also instrumental for issues involving electronic transitions (optical and electronic properties) and cases in which electrons are moved (such as reactions) as classical force field methods cannot be used.

Almost all of the simulation methods described will make use of classical force field molecular mechanics (MM) and molecular dynamics (MD), with a focus on developing methods or strategies that can be used for material development. Force fields which describe the bond and non-bond characteristics of the atoms are an important part of classical molecular modeling. Today many different force fields are available depending upon the software package, and new force fields are continually being developed today. In several examples in this chapter, the consistent valence force field (CVFF) [6] was applied, which is one of the older force fields, while in other examples, the polymer consistent force field (PCFF) [7] was used. All force fields will describe both the bond and non-bond character of the atoms and their linkages; see e.g. [8]. Without going into detail, the force field should contain terms which describe bond stretch, angle bend, rotational bond torsion, distortion out of

plane, longer range issues (such as one to three interactions), as well as any cross-interaction between these terms. The non-bond description will involve van der Waals (or Lennard-Jones) and Coulombic interactions. Depending upon the force field and software used, some of the parameterizations may be further edited for customization, or new force fields may be accessed. For the engineer, these force fields merely represent constitutive relationships between the atomic and molecular forces and the atomic positions, or material structure. The difficulty in using molecular modeling then becomes one of level of trust in the force field. There are also trust issues related to the definition of the structure trying to be modeled, but that may be handled by modeling ranges of structures to get an idea of the possible response range. For this reason, it is always best practice to compare the model against experiments to be sure the chosen force field is robust enough. Benchmarks or experimental validation is highly desired to ensure confidence in the modeling results and is especially needed when the results must be used in product development.

Until length-scale bridging methods are fully developed which allow transparency forward and backward from molecular to macroscale (refer to the Discussion section of the preceding chapter), one of the most effective uses of molecular modeling is through the use of relative trends. As a tactic, it is one of the fastest as validation in terms of trends to the experimental result is faster than trying to model all aspects of the explicit material. Also in many cases of commercial materials, the components themselves are not atomistically well defined. Since the molecular model is confined to small length scales, almost all molecular modeling can be considered as a nano-material perspective, and the comparative analysis is a good approach from which connections to macro-material trends may be developed.

In most of the provided examples, the strategy involved is to generate comparative molecular interactions in order to develop directional trends, with the philosophy that every property or performance metric is derived from a series of interfacial interactions that respond through the bond and non-bond forces that manifest in energy and structural changes. This philosophy serves the molecular modeler well, in that by concentrating on compositional interactions, the most important ones that contribute to the mechanical response can be identified early. The interfacial interactions may be defined as self-to-self (cohesive types), or self-to-other (adhesive types), but the general strategy is always the same: that of understanding basic pairwise interactions that serve to explain a macro-phenomenon.

Since the fastest way to obtain the family of interactions is with trend analysis (rather than a search for properties), the molecular modeler has latitude to investigate different perspectives that affect the material response within the compositions and molecular structures and architectures. But the models can also look at environmental conditions like temperature, pressure, or moisture and even the rate of change of these conditions. If different perspectives begin to converge on a similar structure or condition, then there is higher probability a root cause has been identified. An interesting example of this kind of modeling investigation for a defect found during commercial use of an IC dielectric which used a combination of techniques was reported in [9–12], but this is not covered in this chapter. In some cases, exact

properties may be derived directly from the molecular model as is the case of modulus which shows remarkable consistency regardless of scale, demonstrating that its main interaction is at a molecular structural level. However, it is always cautioned that benchmark or validation models to experimental results should be done for both trend analysis and property derivation. In cases where electronic properties are involved (and quantum mechanics is used), the philosophy is generally similar, in that no material is felt to be acting in a vacuum by itself and in some way is modified by its environment, even if that environment is represented by a simple molecular pair or a surface.

Since energies and structures are the only two basic results coming out of a molecular model, the setup and definition of the base model are of primary importance as it will provide the basis for comparison. This base model will vary depending upon the material system and the performance properties that are being developed within the application. And even in cases where the method is not quite in sync with the application, the trends found can be used for initial analysis to understand how the molecules are responding to whatever stress is applied in order to design a better model (or material). In many cases, the major material components are used with modifying agents to simplify the base model. Additional components that increase the model size may be added depending upon the time allotted to solve the issue and computer resources available. Both stoichiometric and nonstoichiometric models can be used although the danger is always whether large enough ranges have been used in order to bound the composition variable space. However, ranges can also be quickly pared down by the experimentalists' experience with similar formulations or materials or from scoping models of specific components.

### ***4.1.3 Scope of the Chapter***

Without trying to be inclusive with all of the possible simulation methodologies that can be developed, this chapter tries to show the utility that molecular modeling can bring to the material developer and to the material integrator dealing with electronic packaging issues. The different examples will demonstrate that the appeal of molecular modeling is not necessarily the methods available within a software package, but the versatility that can be accomplished with basic tools to create methods directed at specific material applications. Several sections discuss the prediction of bulk and interface properties by means of atomistic modeling. However, property predictions are just one part of molecular modeling, and for the work described here, we will discuss another less acknowledged area of simulation. The former is distinguished from the latter through the concept that often the time-dependent evolution of properties of interacting material systems is needed, so how these molecular interactions evolve is important in order to make a rational judgment of performance worthiness from the material composition perspective. Molecular modeling provides a means to simulate and judge the relationship between the

chemistry (and chemical composition) and the performance of the interacting materials. Such interactions, or interfaces, will often have properties of their own that can be classified using molecular modeling simulation. Examples will be provided which will discuss how current software is being used to scale from the molecular into the nano-/microscale through the use of coarse-grained (CG) or mesoscale models (which coarse-grain parameterizes molecular models to larger particles in order to derive a scale-up in model size) in order to begin to address the small scale weaknesses of molecular modeling. Most of the modeling examples that will be discussed represent the actual materials being developed for electronic packaging.

The chapter starts with a short recap of molecular dynamics (MD) theory, after which the first example covers the prediction of thermomechanical properties of an epoxy molding compound (EMC) and the adhesion properties of an EMC/copper interface by means of MD and CG MD approaches. The second case will review the work done for die attach and via fills, covering the modeling of wetting, adhesion, and reliability cycling. The third case discusses model scaling to discrete element modeling (DEM) for understanding underfill flow. The work done using DEM is not fully molecular modeling per se, but the energy relationships were identified by molecular modeling, and the repercussions of the right energy relationships are discussed. The next example stays within the area of model scaling, reviewing work done in mesoscale (CG) modeling of an epoxy molding compound which relates to the first example. The fifth example covers the molecular modeling of some silicate layers used in planarization and encapsulant layers for flat panel displays. The next example is another mesoscale CG-related one, exploring simple diffusion of organic bases which is of concern to photoresist poisoning. As a cautionary note, any representation of the materials are for illustrative purposes only, as actual compositions cannot be shown. Although all of the molecular models and the coarse-grained models shown were done in 3D, 2D views are shown here for simplicity. The final example reports the prediction of thermomechanical properties of a low-k dielectric material, SiOC:H. The chapter ends with conclusions and acknowledgments.

## 4.2 Concise Overview of Molecular Dynamics

The focus of this chapter is not to provide an elaborate in-depth overview of molecular dynamics as excellent textbooks on this topic are readily available (e.g., [8, 13–15]). Here, a concise overview is given.

From quantum mechanics point of view, matters have dual natures: particle and wave. However, while the geometry of the system is large enough, the wave nature of individual components becomes unapparent and the system becomes determined. When the wave nature of the particle will be ignored or considered implicitly by the potential functions, MD exhibits high efficiency in the simulation of the molecules. MD, widely used in organic chemistry, is a framework for many particle problems and “describes the time evolution of a set of interacting atoms by integration their

equations of motion” [13]. This method assumes the atom(s) as rigid particles of which the movement is described by coordinate variables. The interactions between the particles are described by the potential functions (or force fields). MD is based on Newton’s second law of motion:

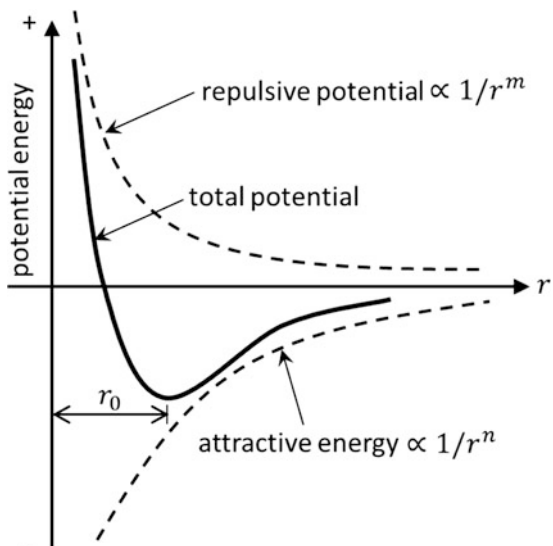
$$\mathbf{F}_i = m_i \mathbf{a}_i \quad (4.1)$$

for each particle  $i$  in a system constituted by  $N$  particles. In (4.1),  $m_i$  is the mass of particle  $i$ ,  $\mathbf{a}_i = d^2\mathbf{r}_i/dr^2$  is its acceleration, in which  $\mathbf{r}_i$  is the atomic position, and  $\mathbf{F}_i$  is the force acting on the particle. Therefore, MD is a deterministic technique: given an initial set of positions and velocities, the subsequent time evolution can be determined. The interaction force between particles, as required in (4.1), can be defined by potential functions or force fields:

$$\mathbf{F}_i = -\frac{\partial}{\partial \mathbf{r}_i} U(\mathbf{r}_1, \dots, \mathbf{r}_N) \quad (4.2)$$

where  $U(\mathbf{r})$  is the potential function. Potentials can be categorized broadly as (i) pair potentials, (ii) empirical many-body potentials and (iii) quantum mechanical potentials. Two-body potentials, such as Lennard-Jones,  $U(r) = 4\epsilon[(\sigma/r)^{12} - (\sigma/r)^6]$  ( $\epsilon$  is the depth of the potential well,  $\sigma$  is the distance where energy equals zero [16]), and Morse potentials,  $U(r) = D\{\exp[-\alpha(r - r_0)] - 1\}^2$  ( $r_0$  is the equilibrium distance,  $\alpha$  is the elastic modulus, and  $D$  is the cohesion energy [17]), are used for large-scale simulations where computational efficiency is a significant factor. Note that (4.2) indicates that the force in each particle depends on the positions of all particles in the system. A typical two-body potential is illustrated in Fig. 4.1. When the distance of the two-body system is larger than the equilibrium distance (denoted by  $r_0$ ), the

**Fig. 4.1** Illustration of a two-body potential function



attractive energy, governed by Coulomb's law, is significant. The attractive energy will fade out when the distance approaches infinity. On the contrary, when the distance of the two-body system decreases, the repulsive energy which is governed by the Pauli exclusion principle will increase. Moreover, the energy approaches infinity if the distance approaches zero.

For systems where multibody interactions are important, the Stillinger-Weber [18], Tersoff [19], and Brenner potentials are often used. Such potentials are empirical in that they are parameterized by fitting either to a set of experimental measurements or to quantum mechanical calculations. However, large local departures from the coordination or bonding used for the parameterization can take such potentials outside their domain of validity and lead to unreliable results. This has fostered efforts for deriving interatomic potentials directly from quantum mechanical principles.

Equation (4.1) represents the system at specific time  $t$ . To understand the interaction of the particle and the mechanical response, a method regarding the time integration should be used. The most common time integration algorithms are based on finite difference methods. Two popular integration methods for MD are the Verlet and predictor-corrector algorithms [15, 20]. The integration time step must be small enough to capture the dynamics of the vibration modes of the system, with frequencies in the order of  $10^{13} \text{ s}^{-1}$ . Each particle which is described by MD has three degrees of freedom, which can be either fixed or free. For a system with billions of particles, periodic boundary conditions (PBC) (see, e.g., [13]) can be used to reduce the computational effort.

The initial conditions of the MD simulation include the definition of initial coordinates and velocities of particles in the system. The coordinates can be obtained from stoichiometry, measured by experiments or ab initio computational methods. The initial velocity can be defined by the temperature, which is directly related to the kinetic energy by the equipartition formula  $K = 1.5Nk_B T$  where  $N$  is the number of particles and  $k_B$  is Boltzmann's constant. The summation of the kinetic energy of each particle in the system obeys the equipartition formula. Moreover, the centroid velocity equals the given system velocity or zero if the system is at rest.

In principle, MD is based on the theory of classical mechanics while considering the interaction between atoms. MD can be applied when the wave nature can be ignored or represented implicitly. A simple test of the validity of the classical approximation is based on the de Broglie thermal wavelength:

$$\Lambda = \sqrt{\frac{2\pi\hbar^2}{Mk_B T}} \quad (4.3)$$

where  $M$  is the atomic mass, and  $\hbar$  is Plank's constant. If  $\Lambda \ll a$ , where  $a$  is the nearest neighbor separation, the assumption of the classical approach is satisfied. However, for very light systems, like H<sub>2</sub>, He, Li, or a system with sufficiently low temperature, the criterion is not satisfied, and hence, quantum effects will become important.

## 4.3 Computing Thermomechanical Properties of Cross-Linked Epoxy and Epoxy/Copper Interface

This section deals with the calculation of the thermomechanical properties of an epoxy molding compound formed by curing tri-/tetra-functionalized EPN1180 with bisphenol A, i.e., the “Delft compound” [21]. Conducting MD simulations of polymeric materials is not straightforward as, unlike in crystalline solids, the molecules in polymeric materials are more or less randomly connected, which is particularly true for polymers with cross-linked network structures. Early work mostly concentrated on the network build-up process through Monte Carlo simulations on idealized models, without considering chemical details [22]. More recently, atomistic representations of polymer networks were proposed along with realistic and validated force fields [23, 24]. More advanced methodologies involve dynamic curing of networks starting from a physical mixture of monomers. Yarovsky and Evans [25] applied a cross-linking scheme for epoxy resins. Other authors proposed multistep procedures to create covalent bonds and iteratively equilibrate the structure. For instance, Wu and Xu [26] constructed a model by repeatedly cross-linking and relaxing the system until the desired conversion rate was reached. Similarly, Varshney et al. [27] used a cyclic cross-linking algorithm including multistep topology relaxation to construct an epoxy-based polymer network. Based on the molecular models built by the afore-described approaches, MD simulation techniques were used to simulate the dynamic [28], thermal [23, 27, 28], mechanical [23, 29, 30], and diffusion [24, 25, 31] behavior of epoxies and epoxy-based composites. Alternatively, Kacar et al. [32, 33] developed a mesoscopic approach to predict properties of cross-linked epoxies and epoxy/aluminum interfaces by effectively combining dissipative particle dynamics (DPD) with MD employing the polymer consistent force field (PCFF) [7].

In this section, a cross-linking-relaxation methodology is presented which allows the construction of a highly cross-linked polymer network from a given set of monomers. By using an existing PCFF [7], several thermomechanical properties of the model epoxy are computed such as the coefficient of thermal expansion, glass transition temperature, Young’s modulus, and Poisson’s ratio. More details can be found in [34].

### 4.3.1 MD Epoxy Model Generation

The model material studied in this work is an epoxy phenol novolac (EPN). The EPN consists of EPN 1180 as epoxy and bisphenol A (BPA) as hardener [21], shown in Fig. 4.2. Using the stoichiometric mixing ratio of tri-epoxy/tetra-epoxy/BPA = 2:3:9, the theoretical full conversion can be reached, and the average epoxy functionality of 3.6 is maintained.

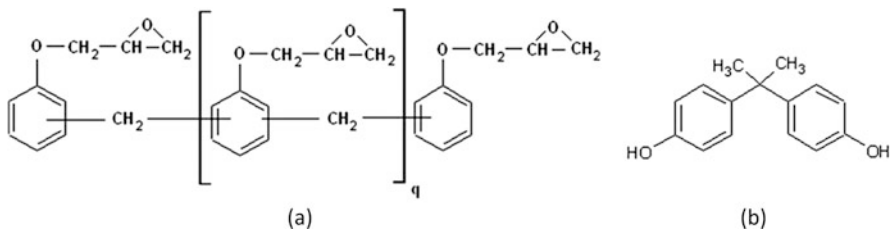


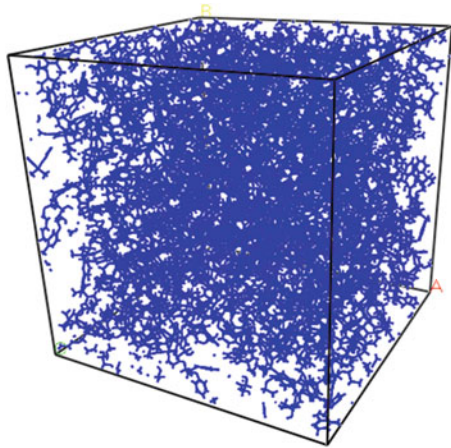
**Fig. 4.2** Molecular structures of (a) epoxy and (b) hardener [21]

To describe the interactions between atoms in the molecular model, the PCFF [7] is applied. This PCFF has been parameterized and validated for various organic and inorganic species and consists of valence terms (bond stretching, angle bending, dihedral and improper interactions, and cross-coupling) and non-bond terms (electrostatic and van der Waals forces):

$$\begin{aligned}
 E_{total} = & \sum_b \sum_{n=2}^4 k_n(b - b_0)^n + \sum_\theta \sum_{n=2}^4 H_n(\theta - \theta_0)^n + \sum_\phi \sum_{n=1}^3 V_n(1 - \cos n\phi) \\
 & + \sum_\chi K_\chi \chi^2 + \sum_{b, b'} F_{bb'}(b - b_0)(b' - b'_0) + \sum_{b, \theta} F_{b\theta}(b - b_0)(\theta - \theta_0) \\
 & + \sum_{\theta, \theta'} F_{\theta\theta'}(\theta - \theta_0)(\theta' - \theta'_0) + \sum_{b, \phi} (b - b_0) \sum_{n=1}^3 V_n \cos n\phi \\
 & + \sum_{\theta, \phi} (\theta - \theta_0) \sum_{n=1}^3 V_n \cos n\phi + \sum_{b, \theta, \phi} F_{b\theta\phi}(b - b_0)(\theta - \theta_0) \cos \phi \\
 & + \sum_{i, j} \frac{Q_i Q_j}{r_{ij}} + \sum_{i, j} \epsilon_{i,j} \left( \frac{A_{ij}}{r_{ij}^9} - \frac{B_{ij}}{r_{ij}^6} \right)
 \end{aligned} \tag{4.4}$$

The parameters in this model are explained in more detail in [7, 34]. The most challenging aspect of constructing the molecular model is how to accurately describe the cross-linked network of polymers. The actual curing process of thermosetting polymers, which results in the cross-linked network, is complex and involves the formation and breakage of covalent bonds and hydrogen transfers. Depending on the temperature, the curing time required to reach full conversion may range from tens of minutes to hours, which is clearly not feasible for MD simulations. For this reason, a methodology was developed that yields the final cross-linked structure without actually simulating the details of the chemistry of the curing process [34]. In order to achieve a fully relaxed network, the cross-linked system is further equilibrated by MD simulations under the canonical (NVT) ensemble at 600 K for 1 ns, followed by NVT annealing to 300 K at a cooling rate of 10 K/10 ps. Afterward, another MD simulation is performed under the NPT ensemble for 1 ns at 300 K and atmospheric pressure to bring the system to the correct density. An example of the cross-linked structure for the studied epoxy resin is shown in Fig. 4.3, for a conversion rate of 90%.

**Fig. 4.3** An example of the molecular configuration after cross-linking to a conversion rate of 90%



### 4.3.2 MD Epoxy Model Results

First, volume shrinkage caused by cross-linking is calculated. To this end, systems generated along the trajectory of the polymerization simulation, with conversions of 0%, 25%, 50%, 75%, and 90%, were equilibrated at 300 K. The obtained cell volume for each conversion is shown in Fig. 4.4a, including the volumetric shrinkage with respect to the uncross-linked state. For the highest cross-linked system (90% conversion), a volume shrinkage of 4.24% is predicted. It can be observed that volume shrinks consistently with cross-link density [34]. In order to study the temperature dependence of various thermodynamic quantities, a high temperature annealing protocol was followed. The temperature was first increased to 500 K and equilibrated for 500 ps using an NPT ensemble under atmospheric pressure and incrementally decreased to 200 K. At each temperature, the system was equilibrated by an NPT MD simulation at atmospheric pressure for 200 ps. For each temperature, the volume was monitored over the entire duration of the simulation. The thus obtained volume versus temperature curve is depicted in Fig. 4.4b. The discontinuity in the volume versus temperature slope corresponds to the glass transition temperature  $T_g$ . To determine  $T_g$  from volume versus temperature data, segmental linear regression was conducted and depends on the selected temperature range. Bandyopadhyay et al. [35] derived  $T_g$  as a temperature range based on five choices of temperature ranges for data fitting.

The volumetric coefficient of thermal expansion (CTE)  $\alpha$  is defined as

$$\alpha = \frac{1}{V_0} \left( \frac{\partial V}{\partial t} \right)_P \quad (4.5)$$

with  $V_0$  the equilibrated volume before the cooling simulation starts. From Fig. 4.4b, the CTE of the cured (90%) epoxy is calculated as 191 ppm/K in the glassy state and

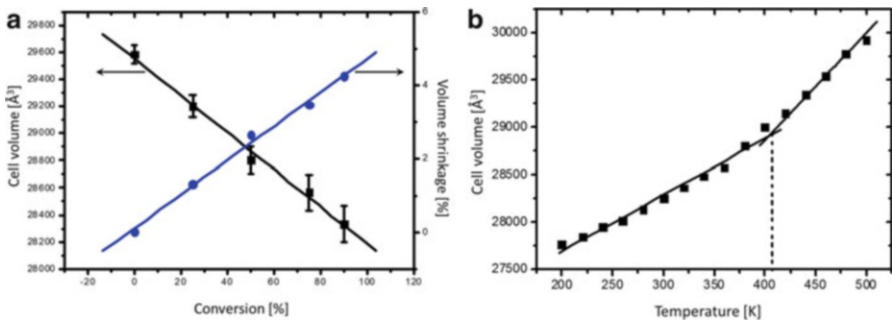


**Fig. 4.4** (a) Volume shrinkage as function of conversion and (b) cell volume as function of temperature (the dashed line indicates  $T_g$ )

397 ppm/K in the rubbery state, which are in good agreement with experimental values of 210 ppm/K and 570 ppm/K [21].

Calculation of mechanical properties through molecular simulations usually follows one of three methods, namely, static, dynamic, or fluctuation approaches [34]. To extract the elastic properties of the epoxy molding compound, the dynamic method is applied. To this end, a tensile loading is prescribed onto the molecular model which is a much larger model than is needed for structural and thermal analyses, for the sake of reducing noises in the engineering stress data. A model having 240 3-mers, 360 4-mers and 1080 BPAs (corresponding to 82,992 atoms) was constructed and corresponds to a cell length of  $\sim 95.50 \text{ \AA}$ . The computational cell along the loading direction was continuously elongated, while the atmospheric pressure was maintained on the lateral surfaces. Due to Poisson's effect, the simulation cell shrinks in the directions transverse to the tensile axis. The strain rate applied in the MD simulation was  $1.10^9 \text{ s}^{-1}$ . This rate is typical for MD simulations but is clearly much higher than used in quasi-static tensile tests. Figure 4.5a shows the stress-strain curve of the 90% cured system at room temperature (300 K). Observe that the lateral stress indeed remains approximately zero. The longitudinal stress exhibits a linear elastic regime up to approximately 5% strain. The Young's modulus was extracted by performing linear regression on this part of the raw stress-strain data. The uncertainty is due to the different choices of strain range used for the linear regression. In this work, the strain range used is  $[0, \varepsilon_{el}]$  with  $\varepsilon_{el}$  varying from 2% to 5%, which gives Young's modulus of  $2.517 \pm 0.168 \text{ GPa}$ , which correlates well with the experimental value of 2.25 GPa [21]. The compressive lateral versus longitudinal strain relationship is plotted in Fig. 4.5b. The Poisson's ratio can then be extracted from the data by linear regression. Following the same approach used for the modulus, we found that the Poisson's ratio is  $0.375 \pm 0.0048$ , falling in the range of 0.30–0.46 for typical glassy state thermosetting polymers. The effect of conversion rate, strain rate, and temperature on the properties is given in [34].

In spite of the extensive use of MD simulations in predicting material properties, these models suffer from severe limitations in length and time scales, which restrict their applications in describing physical processes requiring larger temporal and

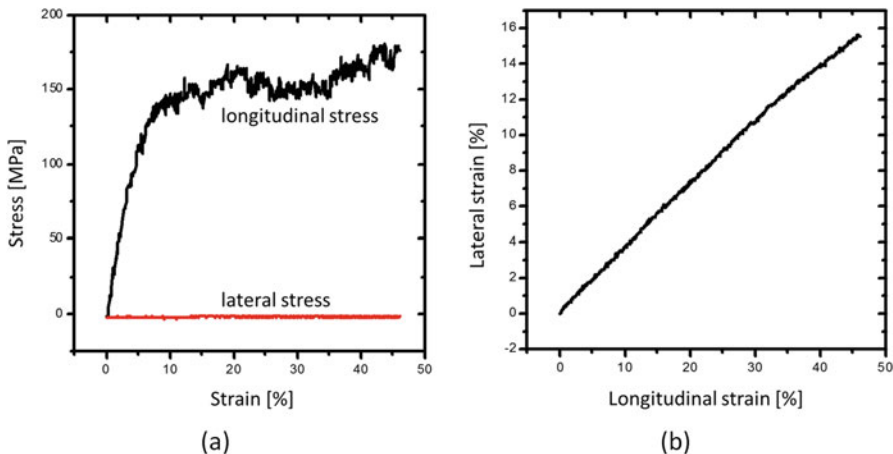


**Fig. 4.5** (a) Stress-strain response and (b) compressive lateral versus longitudinal strain curve for the 90% cured epoxy model at 300 K, using a strain rate of  $1.10^9 \text{ s}^{-1}$

spatial scales to correctly capture, e.g., mechanical responses of polymers. Aside from achieving upscaling in spatial and temporal domains, describing bond rupture for the purpose of modeling material failure and possible cohesive fracture mechanisms in biomaterials is missing in most of the fully atomistic models for polymer networks. In fact, the harmonic or quartic-polynomial bond stretching term present in the consistent valence force fields, such as CVFF [6] or PCFF [7] and (4.4), inherently forbids smooth cutoff of bond energy. Furthermore, valence bond breakage at the atomistic level involves complex re-equilibration of partial charges. Coarse graining (CG) is a method of achieving upscaling by lumping a group of atoms into a “super-atom.” As a result, the number of degrees of freedom is reduced, and larger time steps can be taken in the simulation, due to the softer interparticle interactions. This method consists of two steps: (1) partitioning the system into larger structural elements and (2) constructing force fields to describe the inter-bead interactions. The second step is highly material and application dependent thus does not follow a universal rule.

One of several coarse-graining approaches is to match the physical properties of the material by optimizing parameters of presumed mathematical formulations. For instance, the “Martini” force field [36] was parameterized by reproducing the partitioning free energy between polar and apolar phases of a number of chemical compounds. Shinoda et al. [37] developed a coarse-grained potential for surfactant/water systems by fitting density and surface tension. This approach will be applied here.

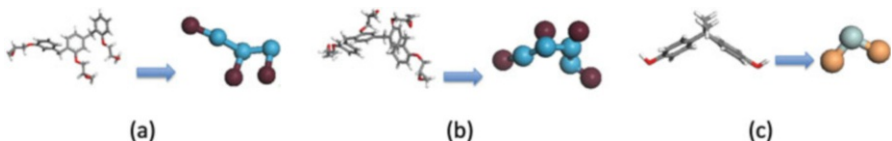


**Fig. 4.6** CG-based bead-connector representations of monomers: (a) EPN-3mer; (b) EPN-4mer, and (c) BPA

### 4.3.3 CG Epoxy Model Generation

In the CG model, the monomers are represented by beads connected by chains that preserve similar geometry as their realistic atomistic configurations. Different monomer structures are mapped onto different bead-chain structures as illustrated in Fig. 4.6 [38]. Epoxy monomers (i.e., EPN-3mer and EPN-4mer) and the hardener monomers are mapped into reactive beads. During the MD simulated cross-linking process, bonds are continuously introduced between these two types of beads.

The non-bonded interactions between beads are described by the widely used Lennard-Jones (LJ) potential:

$$U_{LJ}(r) = 4\epsilon \left[ \left( \frac{\sigma}{r} \right)^{12} - \left( \frac{\sigma}{r} \right)^6 \right] \quad (4.6)$$

where  $\sigma$  is the finite distance at which the interparticle potential is zero, and  $r$  is the inter-bead distance (see Fig. 4.1). The truncation distance for  $U_{LJ}$  is set to  $2.5\sigma$ . The bonded interactions between beads are described by a quartic function of  $r$  and a repulsive LJ function, with a cutoff at  $2^{1/6}\sigma$  [39]:

$$U_b(r) = U_0 + k_4(r - r_c^2)(r - b_1 - r_c)(r - r_c)H(r_c - r) + 4\epsilon \left[ \left( \frac{\sigma}{r} \right)^{12} - \left( \frac{\sigma}{r} \right)^6 + \frac{1}{4} \right] H(2^{1/6}\sigma - r)H(r_c - r) \quad (4.7)$$

where  $H(x)$  is the Heaviside step function,  $k_4 = 1434.3\epsilon/\sigma^4$ ,  $b_1 = -0.7589\sigma$ , and  $U_0 = 67.2234\epsilon$  [39]. The bond extension cutoff distance  $r_c$  is one of the parameters to be fitted. At  $r_c$ , the potential is smoothly truncated, and the bond is removed from the system (bond breakage). The LJ pair potential (4.6) is turned on between the afore-bonded pair. The angle bending interaction is described by a quadratic function of the bond angle:

$$U_a^i(\theta) = k_\theta^i (\theta - \theta_0^i)^2 \quad (4.8)$$

where  $\theta_0^i$  is the equilibrium bond angle. The index  $i$  denotes the angle type: type 1 corresponds to the angle formed by the three beads in a BPA monomer, with assumed  $\theta_0^1 = 100^\circ$ ; type 2 corresponds to the angle formed by a reactive bead in an EPN and a BPA, with  $\theta_0^2 = 180^\circ$ ; all remaining angles formed by beads within each EPN are called type 3, with  $\theta_0^3 = 180^\circ$ . The assumptions on the equilibrium angles

are based on the geometry of the monomer configurations (see Fig. 4.6). All parameters in the inter-bead potentials are quantified by means of the particle swarm optimization procedure which iteratively minimizes the difference between the CG model and atomistic models. Details of the algorithm are provided in [38].

To generate the epoxy model, CG beads representing epoxy and hardener monomers are randomly seeded in a cubic simulation cell with periodic boundary conditions in all three orthogonal directions. The number of different types of monomers obeys the stoichiometric ratio 2:3:9 for 3mer:4mer:BPA. The assembly is equilibrated under NPT ensemble conditions at the temperature of 500 K with a time step of 5 fs for one million steps. Next, a dynamic cross-linking step is performed. Upon reaching the desired conversion degree, the simulation cell is quenched from 500 to 300 K at  $2.2 \times 10^{10}$  K/s, followed by an NPT simulation of one million steps at 300 K to reach the equilibrium density of 1.183 g/cm<sup>3</sup>. The used simulation cell contains 7,834,220 beads, with size  $\sim 85 \times 85 \times 85$  nm<sup>3</sup> at RT equilibrium.

#### 4.3.4 CG Epoxy Model Results

The cross-linked epoxy material was equilibrated under NPT ensemble conditions at 610 K. Next, the material was cooled down from 610 to 150 K during four million steps, at a cooling rate of  $2.3 \times 10^{10}$  K/s (time step 5 fs). Figure 4.7a shows the specific volume versus temperature for different conversions. From these results,  $T_g$  for the 90% and 0% cross-linked systems is 401 K and 312 K, respectively, which is in good agreement with the values from the MD simulations [34] and Sect. 4.3.2. To verify the validity of the CG model predictions at other conversion rates, Fig. 4.7b shows the CG and MD results in which the error bars correspond to different choices

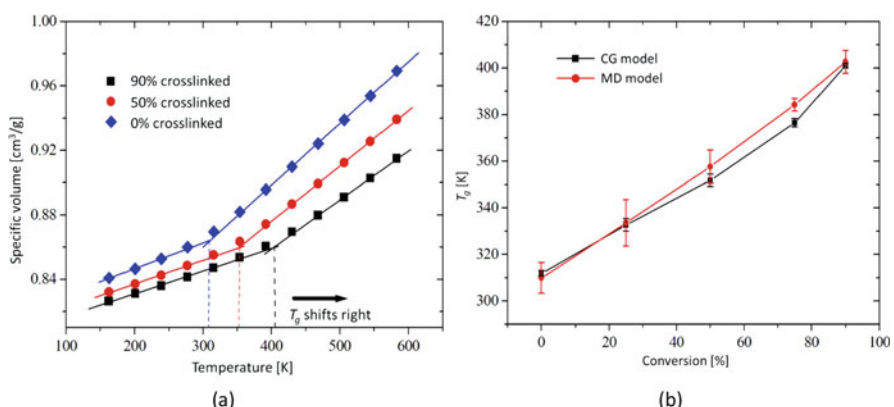
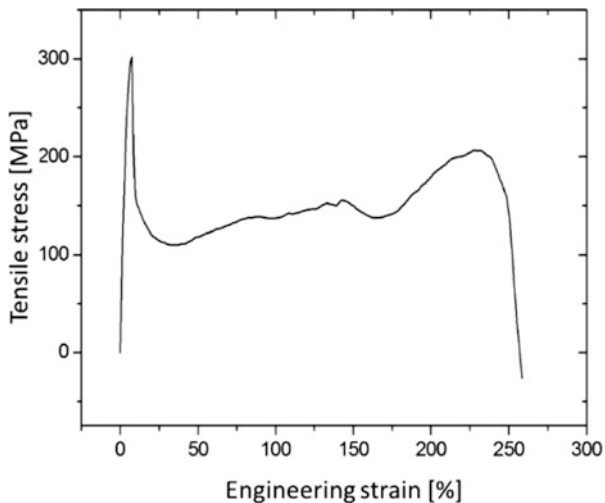


**Fig. 4.7** (a) Specific volume versus temperature relationships for systems with different conversions using the optimized CG potential parameters; (b) glass transition temperature versus conversion relationships obtained from CG and full MD simulations

**Fig. 4.8** Resulting stress-strain curve of the simulated tensile deformation



in temperature range in the bilinear regression. It is seen that the  $T_g$  values as function of conversion predicted by the CGMD model are very close to the values from the MD model [34].

The tensile behavior of the epoxy is simulated by subjecting the cross-linked and equilibrated polymer network to a tensile deformation at 300 K. The deformation is accomplished by elongating the simulation cell along the loading axis with a strain rate of  $10^8 \text{ s}^{-1}$  which is clearly much higher than typical strain rates used in quasi-static loading in laboratory tests. Figure 4.8 shows a stress-strain curve under the uniaxial strain condition. It is seen that at a strain level of  $\sim 7\%$ , the material reaches its yield stress of about 300 MPa. After yielding, the stress immediately relaxes down to  $\sim 110$  MPa [40].

This drastic relaxation is due to cavity nucleation as shown in the first snapshot of Fig. 4.9, where beads are colored by their coordination numbers which is the number of its neighbors within the force field (LJ potential) cutoff distance. The higher the coordination number, the denser the beads are packed. Following this color scheme, the cavities can be visualized in the simulation cell and grow with increasing strain. The stress-strain curve (Fig. 4.8) shows a rather mild strain hardening between 20% and 200% strain. As shown in Fig. 4.9, cavities grow both longitudinally and laterally in this strain regime. The work hardening behavior is a result of the network strands realigning themselves in the loading direction, which yields large strains without significant stress increase. After about 200% strain, most of the network strands are significantly stretched in the loading direction, and the entire simulation cell is changed to a network of ligaments and cavities. Further increasing the strain leads to bond stretching in the ligaments, thereby increasing the stress. Eventually, some of the bonds fail which results in a sequence of bond failure and leads to the final failure of the material by rapid scission of a large number of strands at about 230% strain [40].

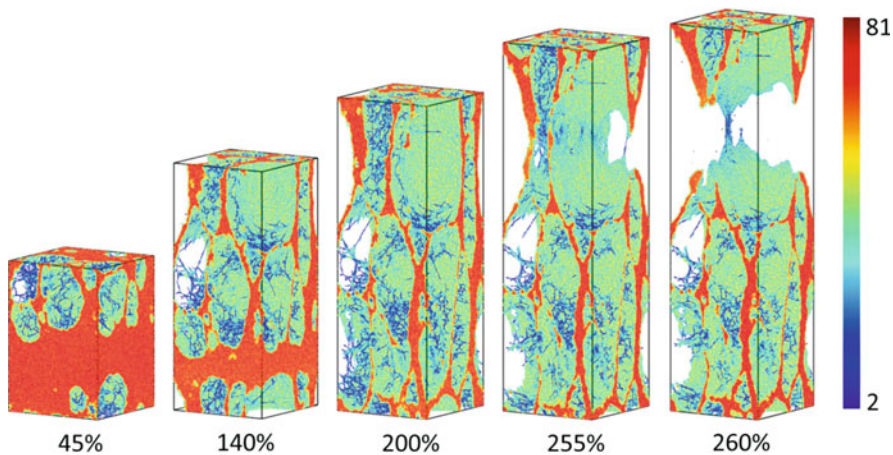


**Fig. 4.9** Snapshots of the deformation sequence. (Generated by Atomeye [41])

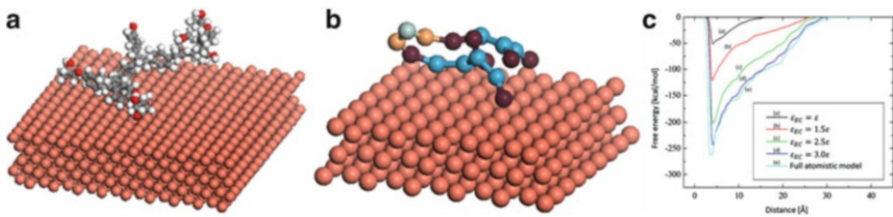


**Fig. 4.10** (a) Atomistic and (b) coarse-grained models of the representative molecule attached to the Cu substrate; (c) Free energy surfaces of the CG model computed using different CG Lennard-Jones parameters, compared to the free energy surface of the corresponding full-atomic model (in the shown graphs,  $\sigma_{EC} = \sigma$ )

### 4.3.5 CG Epoxy/Copper Model Generation

The epoxy molding compound is described by the potentials given in Sect. 4.3.3. The copper substrate is modeled by using the virtual FCC crystalline structure, with an appropriate lattice constant. In [42], the nearest-neighbor distance between the FCC substrate beads is chosen to be  $1.204\sigma$  and corresponds to a lattice constant of  $1.204\sqrt{2}\sigma = 7.463$  Å. In addition, to describe the interactions between the Cu beads and to maintain the crystalline structure of the substrate during the MD simulations, each Cu bead is linked to its nearest neighbors on the FCC lattice site using a spring with a spring constant of  $1000\epsilon/\sigma^2 = 79.04$  kcal<sup>-1</sup> mol·Å<sup>-2</sup> [43].

The CG model for the epoxy/Cu interface is based on an LJ 12-6 potential with parameters  $\epsilon_{EC}$  and  $\sigma_{EC}$  (see, e.g., Eq. (4.6)). These parameters need to be determined from the results of a full atomistic model (Fig. 4.10a, b). Next, the free energy surface of the CG epoxy molecule and Cu substrate system is calculated and depends

on  $\varepsilon_{EC}$  and  $\sigma_{EC}$ . The values are now quantified such that the free energy surface of the CG model matches that of the full atomistic model. Figure 4.10c depicts the free energy surfaces using the CG bimaterial model with different Lennard-Jones potential parameters. Calculations show that the free energy surface becomes very close to that obtained from the full atomistic model when  $\varepsilon_{EC} = 3\varepsilon$  and  $\sigma_{EC} = \sigma$ , where  $\varepsilon$  and  $\sigma$  are the Lennard-Jones parameters for the CG epoxy (Sect. 4.3.3 and [40]). More details can be found in [43].

#### 4.3.6 CG Epoxy/Copper Model Results

The CG epoxy/copper model consists of a rectangular block for the epoxy on a Cu substrate containing four (111) atomic planes. Periodic boundary conditions are used on all the lateral surfaces. The model has a total of 7,964,588 beads, corresponding to a physical volume of  $\sim 89 \times 89 \times 79 \text{ nm}^3$  (at 300 K). The tensile deformation of the bimaterial is simulated by prescribing a vertical rigid-body velocity to the Cu substrate while fixing the very top layer ( $\sim 1 \text{ nm}$  thick) of the epoxy. The prescribed downward velocity corresponds to a strain rate of  $10^8 \text{ s}^{-1}$  in the epoxy block. The temperature is kept constant at 300 K using the Langevin thermostat, which appeared to be critical in maintaining the system at a constant and uniform temperature [43].

The structure of the epoxy near the substrate surface is of great interest for understanding adhesion properties. Figure 4.11a shows a zoomed-in view of the near-interface structure of the epoxy after full equilibration at room temperature. It

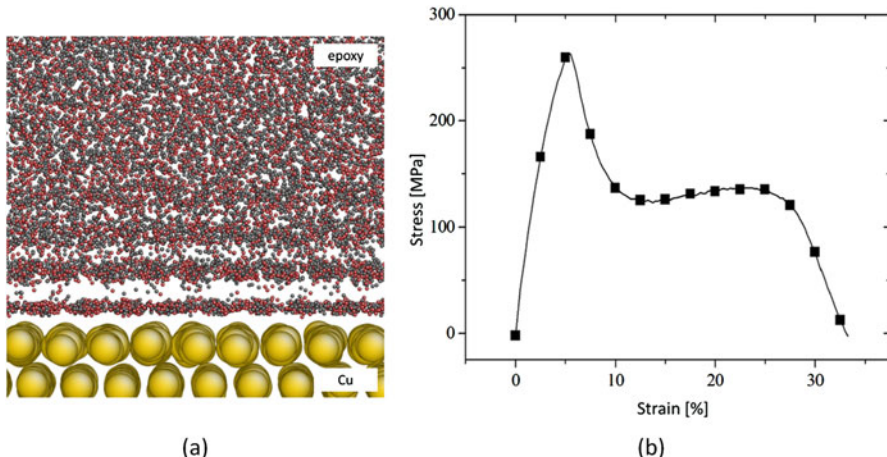


**Fig. 4.11** (a) Zoomed-in view of the interfacial zone. Gray and red beads are the EPN and BPA beads, respectively. Yellow beads are the Cu beads (for better visualization, the epoxy and BPA beads are not drawn to scale); (b) Stress-strain curve for the tensile simulation of the epoxy/Cu bimaterial

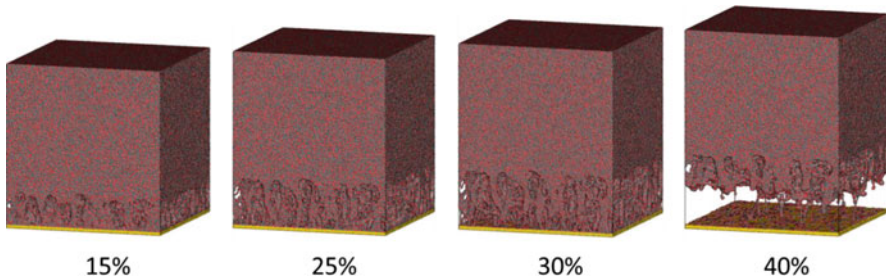


**Fig. 4.12** Snapshots of the deformation process for the 90% cross-linked epoxy/Cu bimaterial under tension

can be observed that the epoxy beads tend to be densely packed into a few distinctive bands. The further away from the interface, the less distinctive the band structure becomes. Such structural feature is due to the rather planar, simplified, geometry of the substrate surface, and the Lennard-Jones interactions between epoxy and substrate beads. Ab initio calculations [44] showed that the benzene rings have a strong adsorption to metal surfaces and prefer to align along the Cu surface. In earlier full atomistic studies of the same epoxy/Cu bimaterial [45], densely packed benzene rings were also observed near the interface. These results confirm that our coarse-grained model for the epoxy/Cu bimaterial correctly capture the structural characteristics of the epoxy/Cu interface.

The obtained stress-strain curve for the strain rate of  $10^8 \text{ s}^{-1}$  is shown in Fig. 4.11b. The curve shows an elastic response until the stress reaches the interface strength of  $\sim 260 \text{ MPa}$  at a strain of  $\sim 5.4\%$ . Subsequently, the bimaterial experiences a drastic stress reduction down to  $\sim 125 \text{ MPa}$  (similar to Fig. 4.8). At about 25% strain, final interfacial failure occurs.

Figure 4.12 depicts several snapshots of the deformed configuration at a strain rate of  $10^8 \text{ s}^{-1}$ . It is seen that at 15% strain, cavities start to nucleate in the epoxy near the interface as a consequence of the relatively weaker force field between the epoxy and the Cu substrate [43]. After reaching the tensile strength and subsequent stress decrease, a weak strain hardening takes place that extends to about 25% strain which is accompanied by cavity growth as well as increased stretching of the polymer strands. Upon reaching the ultimate failure strain of 25%, the epoxy within the interfacial zone is fully stretched. The strong covalent bonds between the polymer beads prevent further deformation in the epoxy. As a result, the polymer strands are pulled off from the Cu substrate as shown in the snapshot at 30% strain in Fig. 4.12. Eventually, this leads to a rather clean interfacial separation between the epoxy and the substrate as shown in the snapshot at 40% in Fig. 4.12.

To study the deformation of the epoxy near the interface region in more detail, the normal displacement as function of the distance from the substrate is plotted in Fig. 4.13a for three different (macroscopic) strain levels. First, the displacement profile prior to yielding (5% strain) is nearly linear, which means that the strain (i.e., the slope of the displacement profile) is nearly constant within the epoxy. Second,

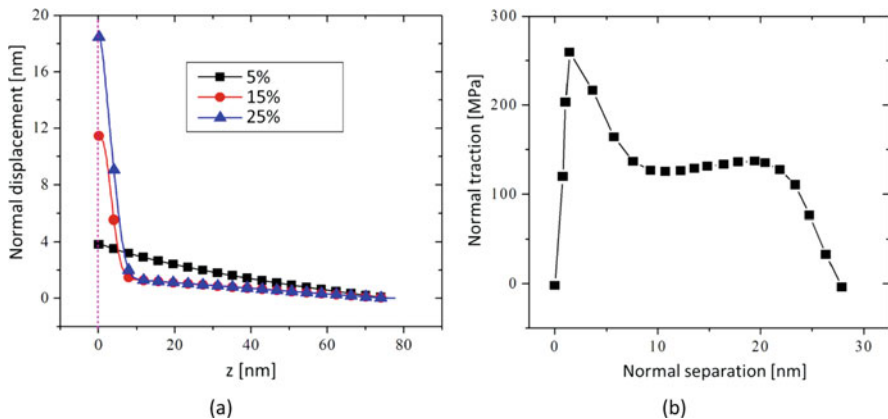


**Fig. 4.13** (a) Displacement profiles along the normal direction for the 90% cross-linked epoxy/Cu bimaterial at three macroscopic strain levels; (b) The extracted traction-separation relationship based on the definition of the interfacial zone

after yielding, the deformation in the epoxy is highly localized to a thin zone of approximately 10 nm near the interface. The average strain inside the interfacial zone is approximately 115% at 15% macroscopic strain and approximately 185% at 25% macroscopic strain. Outside this localization zone, the strain in the epoxy remains at about 2% at both 15% and 25% strain levels. In fact, although not shown, once localization occurs, the bulk strain outside the interfacial zone remains at ~2%, irrespective of the overall strain level. It is remarked that previous full atomistic studies [45] on the same epoxy/Cu bimaterial did not reveal such highly localized deformation. This can be explained by the fact that the material volume used in the full atomistic simulations is smaller than the size of the interfacial zone and therefore unable to capture the localized deformation. This illustrates the necessity of accessing the correct length scale to fully understand the mechanical behavior of polymeric materials and interfaces.

Interestingly, Fig. 4.13a also indicates that the deformed bulk volume during separation increases with increasing strain. This apparent increase of the interfacial zone thickness is entirely due to the increased deformation inside the interfacial zone. The total mass of the interfacial zone remains unchanged. This discovery confirms the applicability of a cohesive zone model in the macroscopic scale where the epoxy/Cu bimaterial is treated as a continuum. It is remarked that this conclusion is not general as the preceding chapter showed that for elastomer/Cu systems, the application of continuum-based cohesive zone models is less straightforward due to the discreteness of the underlying microstructure. For the epoxy/Cu system, the elongation of the interfacial zone thickness can be defined as the separation between the Cu surface and the bulk epoxy at the continuum scale. The relationship between this interfacial separation and the applied tensile stress can be easily obtained by keeping track of the displacement profile at each load increment. As the applied tensile stress equals the traction at the interface, the tensile stress versus separation

relationship gives the desired traction-separation law to be applied in the cohesive zone model at the macroscopic scale (Fig. 4.13b). It can be observed that the thus obtained traction-separation curve shows the general features of traction-separation laws for polymer/metal interfaces. The traction first increases almost linearly with increasing separation. Once reaching its strength, the traction drops drastically, followed by a weak strain hardening until reaching the cohesive strength and critical separation. It is remarked that the cohesive zone model is one of the most commonly used constitutive laws to describe the deformation and failure of materials interfaces (as illustrated in the preceding chapter). However, in most applications, the traction versus separation relationship is assumed ad hoc and calibrated via indirect experimental observations. In contrast, Fig. 4.13b shows a macroscopic traction-separation curve for polymer/metal interfaces which is readily obtained from CGMD simulations at the atomic scale [43]. This perfectly illustrates that, in order to improve the predictive capabilities of material and interface models, tailored multi-scale methods are essential [8, 46, 47].

## 4.4 Wetting, Adhesion, and Molecular Stress Cycling (Molecular Coffin-Manson) for Reliability

In this section, two basic examples will be shown to examine the effects of formulation components on performance. The first example concerns bleed, which is defined as excessive and unwanted wet-out or surface diffusion [48, 49] into areas that interfere with further material integration of the device structure. The second example covers adhesion [50–52], which includes the importance of molecular stress cycling as a molecular analog of the Coffin-Manson response.

### 4.4.1 Wetting

Wetting is the first property of interest when understanding the attraction of the material to its substrate and the final adhesion. Experimentally, contact angle is used to describe wettability, but when a reactive formulation is in question, the contact angle result may be misleading because it will represent the uncured formulation components along with any solvent, diluents, modifiers, or other volatile ingredient used. The same can be said of a polymer in solution. The solvents may help the polymer penetrate better onto the substrate but may misrepresent native wetting quality of the polymer. By contrast, wetting analysis within a molecular model will show whether contact is being made with the substrate of interest as well as the impact of the composition. Since the model compositions can be changed at will, comparisons can be done on the impact of unreacted versus reacted components, as well as the impact of solvents and diluents. Subsequent adhesion analysis is then required to understand the abilities of the cured material to adhere to the substrate.

The first example is wet-out of a solvent-free reactive formulation. In this case the formulation is a die attach, which is a highly silver flake-filled solventless resin system. The die attach under investigation was found to wet-out onto neighboring bondpads in a phenomenon called “bleed.” The phenomenon is simply surface diffusion which is controlled by the surface energies of participants. However, the issue becomes more complicated when the product is expected to perform regardless of the conditions and surfaces, and those conditions are not set by the developer of the die attach. The bleed molecular models were quite simple geared toward the actual tests themselves which measured the spread of a drop of the formulation after a set period of time. A stoichiometric representation of the organic binder portion of the formulation was energy minimized with a block of silver atoms (representing the silver flake filler) in order to represent the formulation. This mass was then introduced to the substrate, and the entire structure was allowed to equilibrate at RT for a set period. For comparison purposes the period of equilibration was kept constant for all cases. The results from the model indicated that it was less important to find the energy equilibration point but more important to keep the timing constant which is more in-line with both bleed and contact angle experiments. Both the substrate and the filler block were fixed to keep the periodic nature of these materials intact.

As may be imagined, because these are molecular models, a realistic filler size could not be represented, but the filler is still represented in the model, as wetting to the filler itself could further modify wetting to the substrate. Because these models targeted trend analysis, a parallel placement of the filler and substrate surface was used in all cases, rather than adding in the compounding influence of geometrical effects between the filler and surface. For die-attach applications, this was a valid assumption as cross sections of die-attached regions of a package showed parallel organization of the silver flake in relationship to the surface. The binder wet-out is thus simulated by a combination of both the filler and substrate interaction with the binder. Typically a silver filler was used to mirror the formulation work, but any filler could be used. The substrate material was varied according to the surfaces this die attach may see (silicon, copper, silver, gold, copper oxide, and chromium oxide). Like experimental bleed tests, wet-out using the molecular model was measured as the distance migrated on the surface from the starting mass. An example of the model before and after equilibration is shown in Fig. 4.14. In each picture, the top gray

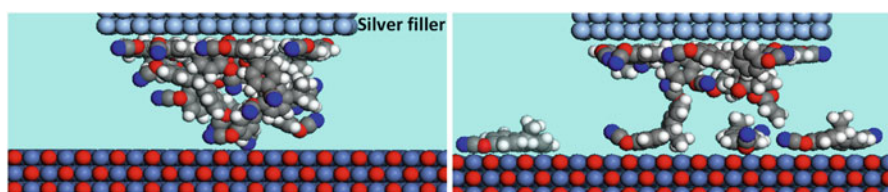


**Fig. 4.14** Example of wet-out of die-attach components before and after RT equilibration. Left, before equilibration; right, after equilibration. The substrate is nickel oxide (red oxygen, blue nickel). The filler is silver (gray silver). For the organic binder, dark blue nitrogen; red oxygen; gray carbon; white hydrogen

block is silver, the bottom layer is nickel oxide, and the binder formulation components are in-between.

The models were repeated with different compositions to give an idea of the compositional effect. Some of the initial results that were compared against experiment are found in Fig. 4.15a, which showed that qualitatively we should be able to tell the difference between a high bleed and a low bleed formulation. While this may be uninteresting to those not involved in bleed or surface diffusion issues, the importance of the model was found when it was discovered that the energy drop found in the model over the trajectory was related to the surface energy of the formulation. A calibration curve back to surface energies was then developed from the extrapolated (surface-free) energy changes in the models (Fig. 4.15b).

The energy drop was then used as a relative gauge of the surface energy of the formulation, and quite quickly trends of the formulation surface energies could be constructed against different formulations and fillers. Figure 4.16a shows that the amount of wetting will drop with an increase in the surface energy of the formulation. The general wetting trend is in keeping with the expectations of wetting theory which says that wetting will not occur if the surface energy is less than the combined interfacial and liquid surface energies [53]:

$$\gamma_s \leq \gamma_{sl} + \gamma_l \quad (4.9)$$

This general relationship suggested that to decrease bleed, a decrease of the surface energy of the substrate or an increase of the surface and interfacial surface energies of the formulation is needed. This relationship was of prime importance to the die-attach formulation developers, as it was quickly acknowledged that of the three surface energy variables, the formulators could only really control the “liquid” effects, i.e., the formulation, including both the binder and the filler (this is primarily because the formulation supplier has no practical design control over the substrates or the other surfaces that the material would see). However the general effect of the formulation is found in Fig. 4.16b which shows that, as the surface energy of the substrate increases, there is an increase in bleed.

#### 4.4.2 Adhesion

Adhesion is another important property for die attach, underfills, via fills, and molding compounds that were under development. Molecular modeling was engaged to understand and improve adhesion, and the simulation technique was a simple one of minimizing a strand of the representative polymer (resin+curatives and any modifying agent), minimizing it to a surface and forcing it from the surface, as represented by the schematic in Fig. 4.17. The distance forcing method employed a simple forcing potential that removed the polymer from the surface by shearing it from the surface. This is a non-equilibrium molecular dynamics method (NEMD), and it was thought to be more representative of the molecular responses to stress

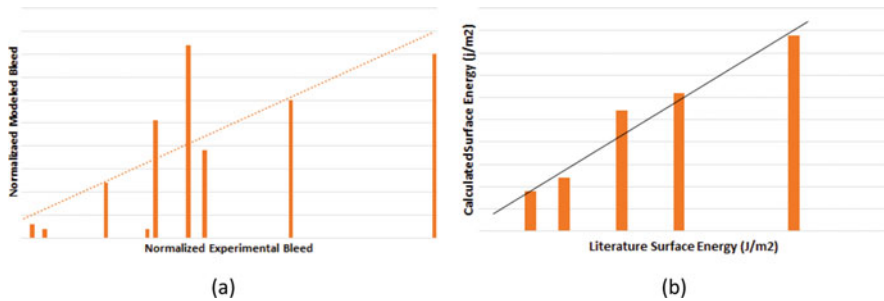


**Fig. 4.15** (a) Actual bleed trends: model vs. experiment; (b) Surface energy calibration curve developed from models of known materials

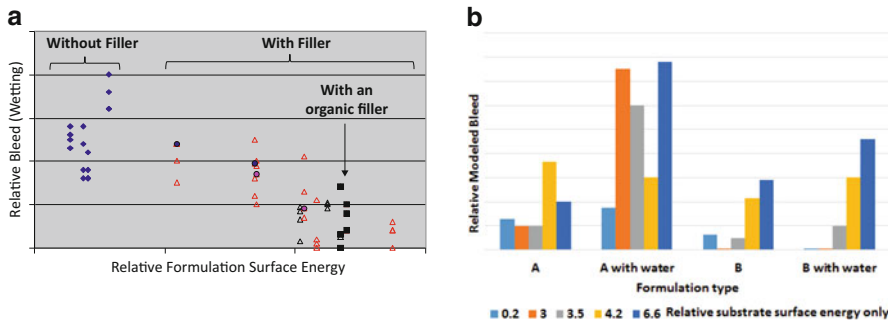


**Fig. 4.16** (a) Wetting vs. formulation surface energy showing general drop in bleed with formulation surface energy; (b) The effect of water on bleed using two different formulations (A is water sensitive and B is not)

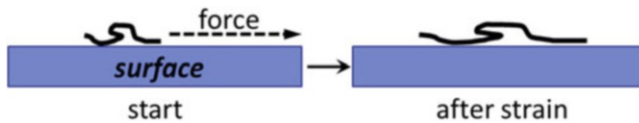


**Fig. 4.17** Schematic of the adhesion model which uses a forcing potential to the end of the binder polymer chain

during use, which can be adjusted depending upon the time scale or evolution under study.

Typically the forcing potential was applied at the end of the polymer chain, or if it was more folded or branched to the end of the long axis, in the direction of the chain axis in order to determine the highest energy resistance to the removal. For cohesion, a dual strand of the polymer was minimized together (the second strand used as the “substrate”) and a forcing potential applied at opposite ends through the center axis, or as close to the center axis as possible, in order to shear the strands apart lengthwise. For all comparisons, the total simulation time was kept constant. It

was rationalized that for polymers, this technique could then follow the time-dependent evolution of the strain with an energy response as a combination of non-bond interfacial forces as well as the bond-bond, bond-angle, and torsion effects that would follow the strain imposed depending upon their interactions and the responses from the parameterizations.

It is worthwhile to point out that because the goal was to develop relative trends than absolute values, the tactic engaged was to find the maximum resistance to separation that the interactions might offer by aligning and stressing in the direction which allowed the highest contact. This was done to maximize the comparison analysis and to help eliminate, or at least reduce, the uncertainty when issues of cure and conditioning are entered into an already complicated variable space. Trial and error showed that lower resistance energies were derived using other forcing directions, suggesting that the adhesion or cohesion of polymers has a maximum interaction footprint that is different depending upon the resin and curative combination. All adhesion comparisons were usually done at multiple rates by increasing the target distance to be accomplished within a set simulation time. The need for understanding rate dependencies was initially rationalized based upon the fact that on a molecular level, there is no guarantee that all atoms are moving at the same rate. It was then found that generally when the maximum energy barrier was plotted against the average model rate, the barrier would increase with rate up to a point when the energy trend would break. The break point was used as the point of maximum possible resistance of the modeled pair interaction (the energy and rate dependency range was found to be important to know, as the low end rate extrapolation could be used for parameterizing coarse-grained diffusion models; see Sect. 4.8).

An example adhesive energy curve is shown in Fig. 4.18a showing that in most cases the molecular trajectory will go through an energy maximum that can be used to estimate relative adhesion strength performance. In addition, the initial slope of the energy-displacement curves could be used to extract the elastic modulus (as with the maximum energy, the modulus was also found to be rate dependent, and a similar energy break was used to determine the highest possible modulus). By running the

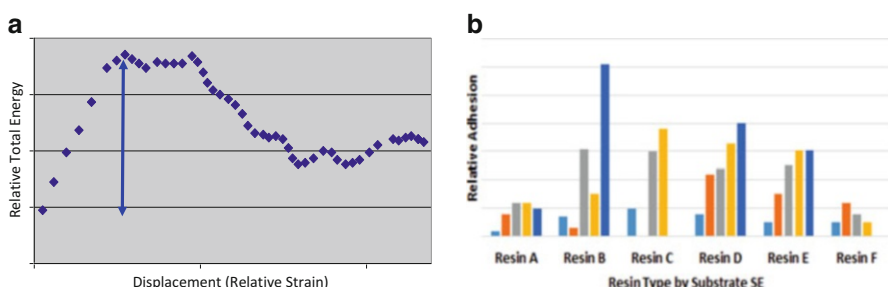


**Fig. 4.18** (a) Adhesion energy trajectory example; (b) Adhesion comparisons of resin candidates plotted against the relative surface energy of the possible substrates the formulation may touch (each group shown is in order of lowest to highest substrate surface energy; the first bar in each group is the cohesive energy)

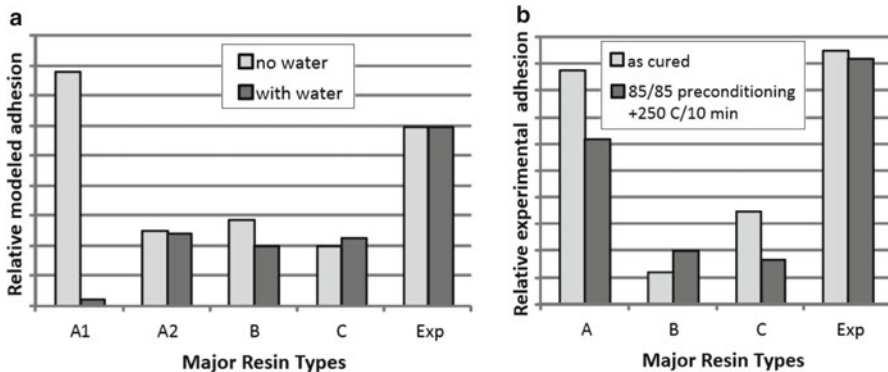


**Fig. 4.19** (a) Simulated vs. (b) experimental adhesion effects of moisture (“Exp” denotes an experimental formulation target under investigation)

simulations on different substrates (which usually ranged from silica to nickel oxide), comparisons of resin candidates could be run for down-selection of the best candidate depending upon the surfaces it might see. Figure 4.18b shows an example of such comparison in which the resin adhesion is plotted against different substrates using their surface energies, showing how different resins might respond with different substrates. This is only one example of model usefulness as the comparison can be used for initial evaluation of resins when faced with different substrate requirements.

Another example of general concern was determining the resistance to moisture of the adhesive formulation. This was, and continues to be, a main issue for long-term environmental stability. The flexibility of the molecular model is demonstrated by being able to easily simulate candidates without water then with water as a modifying agent. Figure 4.19 shows the model results of resins compared for water-resistant adhesives, along with the experimental validation. As can be seen from the comparison, the model adequately predicts that one of our experimental polymers should perform with superior adhesion retention once moisture is introduced, which was verified when testing was done. The laboratory test experiments were run as-cured and after moisture (85 °C/85RH) preconditioning. One of the resins (A1) is severely impacted by water, demonstrating that for that resin there is a significant plasticizing effect with water.

The models were taken further by examining whether molecular modeling could reproduce stress-cycling reliability trends. In these cases, the impact under investigation was determining if molecular cycling could adequately predict long-term performance, as is predicted by Coffin-Manson. As is well-known, the Coffin-Manson equation relates the number of cycles to the strain through an exponential relationship:  $\epsilon = MN^z$ , where  $\epsilon$  is strain and  $N$  is the number of cycles [54]. A log-log plot then gives a linear relationship where reliability can be judged based upon the expected strains experienced. For molecular stress cycling, after the polymer had been stressed, the forcing potential was removed and the whole model was allowed

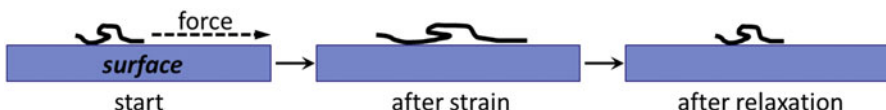


**Fig. 4.20** Molecular stress-cycling schematic

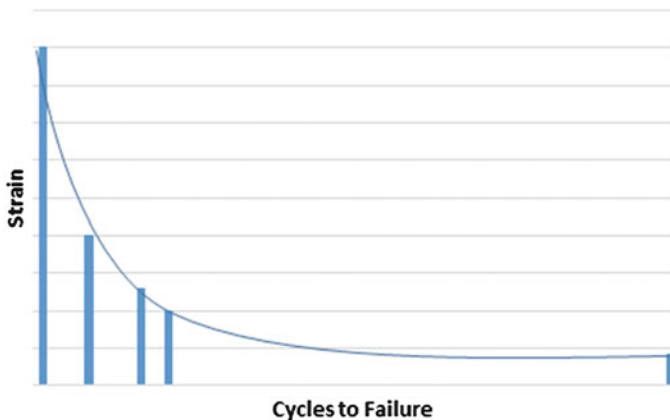


**Fig. 4.21** Schematic of molecular stress-cycling test result showing Coffin-Manson type relationship

to relax as shown in the schematic of Fig. 4.20. This process was repeated until the polymer segments were totally displaced, or no resistance to stress was found in the forcing potential phase.

The molecular cycling was then repeated with different strains until the Coffin-Manson relationship could be built. A simple test case revealed that like experimental reliability tests, the cycles to failure follow a typical exponential relationship (Fig. 4.21) which could be further reduced to a linear relationship by plotting the log of the strain against the log of the cycles.

As moisture reliability has been an important topic to all adhesives (including die attaches, underfills, via fills, and molding compounds), stress cycling was simulated with and without water for new adhesive binders. In addition, both adhesion and cohesion were examined, in order to determine whether cohesive or adhesive failure was more likely. The study involved evaluation of different resins and hydrophobic flexibilizers that may enhance moisture resistance and both the components and formulations were evaluated using the molecular stress cycling. In the interest of time, limited cycling was simulated, and the results extrapolated once a reasonable curve could be generated. The candidates were then plotted against one another by extracting the highest strain sustained at 1000 cycles for relative performance comparison as shown in Fig. 4.22. Modeling comparisons were done on both resins and test formulations, and provided data for our down selection. For instance resin C looked promising to maximize adhesion. However, the modified Formulation A showed both an optimum adhesive and cohesive cycling response.

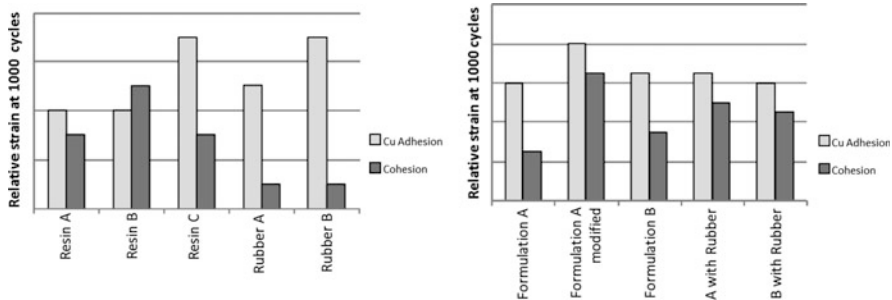


**Fig. 4.22** Resin and formulation selection process based upon the maximum strain that might be sustained at 1000 cycles from molecular stress-cycling simulation

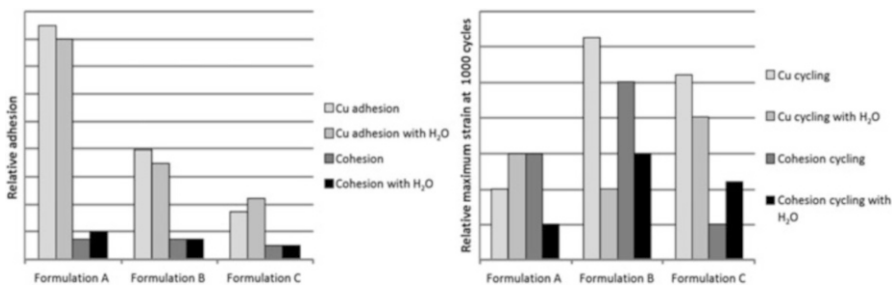


**Fig. 4.23** Effects of moisture for maximum adhesion (left) and maximum strain sustained at 1000 cycles (right)

Formulation work looking for reliability robustness was then aided by modeling the formulated interfaces with and without water. Both adhesion and stress-cycling models were applied in order to get the best idea of possible performance. In parallel, experimental adhesion tests were done both before and after conditioning. The modeled adhesion (Fig. 4.23, left) suggested an adhesion order of A>B>C which was exactly the order of the experimental results. However, after using the molecular stress cycling, Formulation B was found to be the better candidate (Fig. 4.23, right). Experimental adhesion tests after humidity conditioning and cycling showed A~B>C, and after thermal cycling followed by thermal shock B>A>C; B was clearly expected to be more robust, in agreement with the molecular cycling model. So for modeling, using cycling clearly did a better job at predicting which material would be more reliable than the single cycle adhesion model. The need for running cycling tests rather than relying on adhesion tests was also found to be generally true experimentally.

The most convincing test for the validity of molecular stress cycling was found when the modeling was used to evaluate resin and cured structures for a via-fill paste application for boards and packages. In this case, the molecular stress-cycling

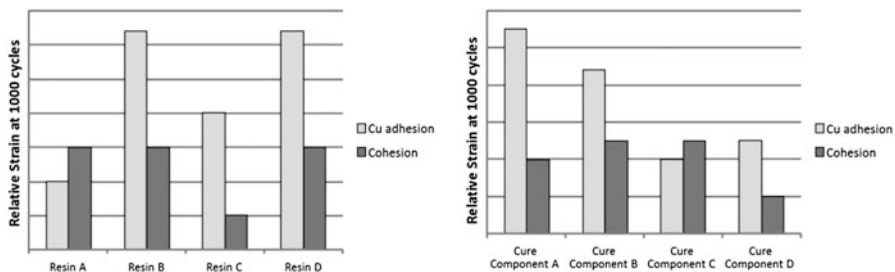


**Fig. 4.24** Molecular stress cycling of possible resins (left) and cured components of the base resin (right)



**Fig. 4.25** Cross sections of vias after thermal cycling (condition B:  $-55$  to  $125$  °C, liquid/liquid immersion, 10 min cycles)

modeling additionally looked at the possible reliability of both the base resin and various cure structures that might form in order to bias the chemistry of the formulation toward the most robust direction (Fig. 4.24).

When vias were actually filled and tested, the new material survived a higher number of cycles under condition B ( $-55$  to  $125$  °C, 10 min cycle) than the competitors at the time. Cross sectioning showed the damage in commercial via fills whereas the new via fill paste showed no damage (Fig. 4.25). This is a good example where the molecular modeling was allowed to participate in the material development process all the way from research concept to commercialization. The combination of simulation and experimental test validation demonstrated that this type of feedback cycle could speed the development and the moisture-resistant die-attach adhesives and via fills were all commercialized (Fig. 4.25).

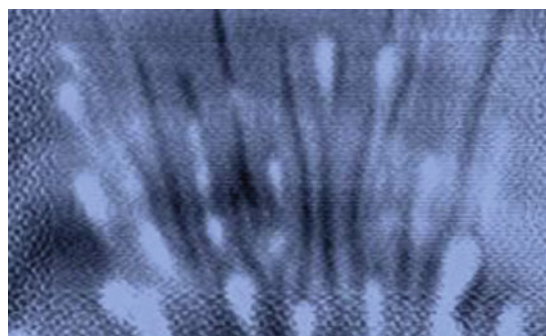
## 4.5 Underfills and First Forays into Scale-Bridging from Molecular Insights

Another interesting application involving both molecular modeling and discrete element modeling (DEM) was looking at variables to improve the filler distribution after the underfill process is complete. Figure 4.26 shows an acoustic image of a bumped die after underfilling showing unwanted streaking signifying uneven particle distribution. The underfill process and material under investigation at the time required capillary flow underneath the bumped die. Today the underfilling process is replaced by other techniques, but this modeling example is included to demonstrate model scaling.

Flow speed, filler settling, filler striation, and voiding are all properties that require a mechanistic understanding in order to improve the materials, which are all at higher length scales than is available from molecular modeling. However, because of the heavy dependence upon surface energy properties for the capillary fill process involved in underfilling to occur, some of the fundamental energies should also have a molecular origin. Although both binder and filler effects on flow are expected from a combination of surface energy and particle dynamics drivers, at the time both could not be implemented into a single molecular model, and a multi-scale strategy was in order. To accomplish this, both molecular modeling and DEM were applied.

For the scaling work engaging DEM, the services of the Particulate Science and Technology Group (under Dr. Masami Nakagawa) at Colorado School of Mines (CSM) apply DEM to understand the effect of the filler particle dynamics within the formulation on the final filler distribution under the die. Like molecular modeling, DEM uses discrete particles and the interactions existing between the particles governed by classic Newtonian physics. However, DEM can also take into account much larger scales than molecular modeling, which can deal with particle shape and distribution, and is an ideal transition example between molecular modeling and continuum methods in order to study a filled composite system. For this study, particle distribution as well as lubrication, drag, and adhesion forces has been taken

**Fig. 4.26** Example acoustic image of filler taken of a silicon die after underfilling (flow direction is bottom to top)



into account and has been discussed in previous articles [55–57], so only the key results will be covered here.

It is known that the spatial distribution and dynamics of particles within a suspension is governed primarily by the forces that act among them as discussed by Bossis and Brady [58]. Most importantly to the impact of molecular modeling was the realization that the particle interactions will for the most part be controlled by the resins of the formulation. These interactions could be derived directly from molecular models. After reviewing the molecular surface energy trends previously calculated using molecular modeling, it was agreed that perhaps a molecularly derived adhesion/repulsion could be derived directly from a molecular model to help represent the dynamics of the filler particles. So the molecular modeling used a modified “bleed” experiment, in which the resin was placed between the filler particle and the substrate, but in this case both surfaces were silica surfaces (to represent the silica filler, but could also represent the oxygen-terminated silicon surface of the die), and the energy drop was monitored while the silica surfaces were stepped closer and closer to one another. In this manner energy/distance curves could be constructed for each binder type, which are shown in Fig. 4.27 for a high and low surface energy binder. These energy curves were the basis of the parameterization of the filler particles for DEM. For the DEM simulation, the major missing parameters were adequate definition of the adhesion, and the energy curves allowed initial estimations of this parameter and adjustment to the governing energy expressions. In this manner, there was no need to explicitly model the binder in DEM, as the binder effect was implicit in the energy relationships. Most importantly, the energy curves gave us a handle back to the composition of the binder.

Two two-dimensional particle flow cases were simulated by DEM. In one case, the effect of speed and particle distribution was studied in order to determine how to control filler settling. The second case explored the reason for uneven distribution found in the acoustic image, in which the filler must flow around an array of solder bumps. The results of the first case involving filler settling are shown in Fig. 4.28. For this case, filler particles with specific particle size distributions were allowed to flow between the top and bottom surfaces. The fluid effects were changed by adjusting the velocity of flow. It was found that the larger particles immediately fell to the bottom, but more mixing of the smaller particles could be found if the flow

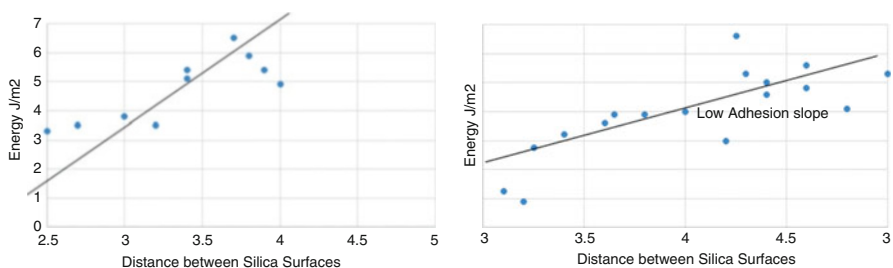


**Fig. 4.27** Energy profile of solid-solid interaction modified by intervening binder. Left: high surface energy binder, high adhesive forces. Right: low surface energy binder, low adhesive forces

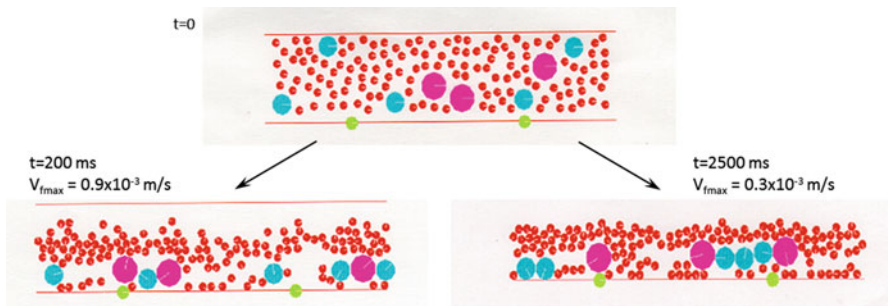


**Fig. 4.28** Effect of flow speed on filler settling and mixing. Top: starting filler distribution before flow. Bottom right: result with flow at higher speed. Bottom left: results with flow at lower speed

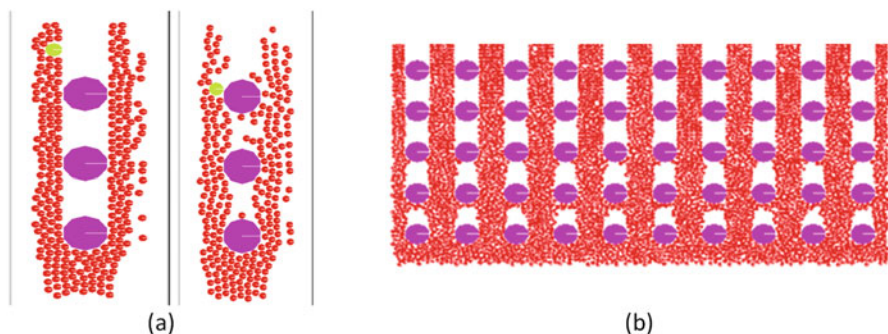
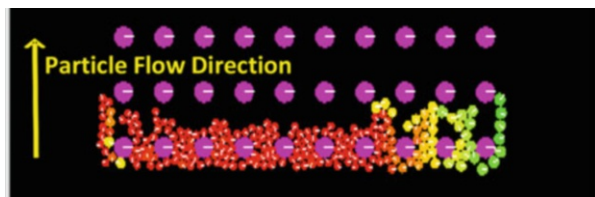


**Fig. 4.29** DEM flow around bumps showing the impact of adhesive forces, flow direction is bottom to top; (a) left, no adhesive forces used; (a) right, moderate adhesion added; (b) no adhesive forces used in a full bump array. The solder bumps are represented by the large circles, and the filler particles are represented by the small circles

speed was reduced. It is the velocity effects that were of interest, as speed would be controlled by the surface energies of the compositions.

The most significant link to the molecular models was found in the second DEM case looking for filler distribution effects. The left picture of Fig. 4.29a shows the case of filler flow if the particles do not contain the adhesive forces in the energy expressions, as does Fig. 4.29b but this time for a full bump array. This simulation did not exhibit the ragged flow found-front found in reality but also did not exhibit any filler filling behind the solder bumps. The right-side picture of Fig. 4.29a shows the end frame of a DEM simulation where adhesive forces have been added, showing filling starting to occur behind/between the solder bumps, but filling is incomplete. Figure 4.30 also shows a bump array simulation with high adhesion forces used. The simulation stopped before very many particles had been injected, due to the agglomeration of filler particles. Also, rather than a straight-line trajectory as found in Fig. 4.29b, more complete filling is occurring behind the solder bumps, as well as an expected

**Fig. 4.30** DEM simulation after unusually high adhesion forces have been added



ragged flow front due to the agglomeration of the filler. The ragged flow front was found from the case that used energies representing high adhesive forces in the DEM.

These simple DEM simulations showed us that to control the flow front and the backfilling behind bumps, the binder had a significant effect on fill distribution mostly due to high adhesive forces.

In follow-on formulations, the high adhesive forces between the silica filler particles were weakened by surface treatment of the filler lowering the surface energies. These formulations showed significantly lower streaking, demonstrating the predictive quality of the scaled DEM models (in another DEM investigation targeting conductive adhesives, an electrical resistive chain model was built based upon contact points after filler compaction. Although the study is not included here, as it does not include molecularly derived forces, this study further demonstrated the role of optimizing filler shape as well as particle distribution based upon particle models [57]).

## 4.6 Scaling the Adhesive Interface Using Coarse-Grained Molecular Models

In this section the scaling from the molecular level to a coarse-grained mesoscale level by direct parameterization of the coarse-grained particles is discussed. This section presents a summary of the findings reported in more detail in [1, 59, 60] and was initiated by a consortium of the EU-funded project NanoInterface (NMP-2008-214371). Here, the main interface targeted for the coarse-grained mesoscale modeling was the copper oxide-binder interface.

Coarse-grained mesoscale models, like DEM and classical molecular dynamics, are particle models which apply the basic Newtonian rules of interaction and movement. The general concept behind coarse graining is to combine groups of atoms into new larger particles or “beads.” Like DEM and molecular modeling, the energy relationships between the particles/beads must be constructed and parameters defined to govern how the particles interact. Typical coarse-grained force fields include the Martini force field [61] which typically uses functional groups as the particles/beads. The beauty of coarse graining is reducing calculation complexity by reducing the number of particle centers that need to be calculated. This simplification lets the modeler accomplish simulations of larger systems faster than using the explicit molecular model representing the same structures. The work in this section

made use of the software Mesocite (Biovia) and the embedded Martini force field. Typically coarse-grained force fields like the Martini force field employ parameterization of simple small functional groups. However in this work a bigger jump in scaling was applied by using the entire repeat unit, in order to test whether scaling could be further jumped by use of a larger bead and to further demonstrate the usefulness of coarse-grained molecular models in the multi-scale hierarchy. It must be cautioned however, that the molecular shape of the potential target bead must be considered as currently all mesoscale “beads” are spherically shaped. For our purposes, the three-dimensional nature of the repeat unit was considered appropriate for scaling to a larger bead and still maintains the correct structural relationships. However, if the structure is more linear, smaller beads might be appropriate. In the future, if the mesoscale software progresses sufficiently, bead shapes can be included so that the functionality of the mesoscale level can be improved in a similar fashion as DEM tools [57] that have shown that particle shape and the interactions between the shapes can be included.

Pictures of the repeat unit are found accompanying the energy diagrams in Fig. 4.31. From these pictures it is easy to see that, in order to represent the repeat unit, at least ten functional group beads are swapped for one repeat unit bead. This simplification enabled models to be built representing formula weights up into the millions, rather than the thousands which is typical for models simulated on a desktop computer. The polymer used in this study was one developed by Delft University, based upon a Novolac epoxy as part of the NanoInterface consortium [21].

The parameterizations for the epoxy have been well-described [1, 59, 60], but it is worthwhile to reiterate the parameters required. As mentioned previously, the general Martini force field was modified which required definition of both bond and non-bond energies. It was found that the most important interactions that needed

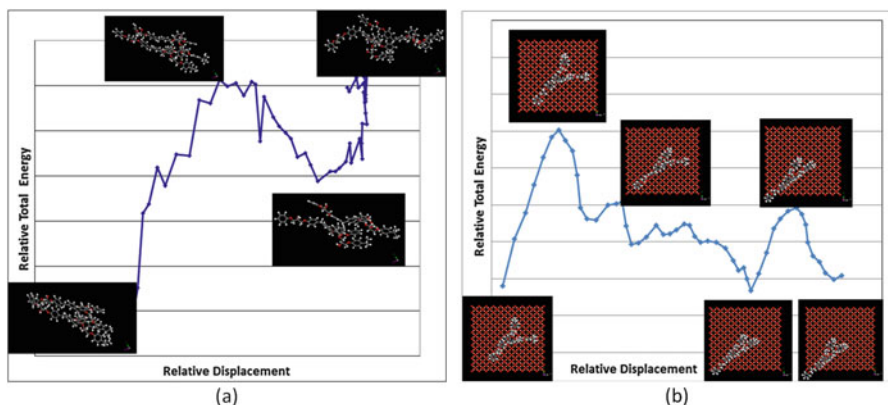


**Fig. 4.31** (a) Example trajectory for parameterizing the cohesive case; (b) Example of adhesive molecular modeling used to determine some of the coarse-grained particle parameters, representing an epoxy on a copper oxide substrate (the view is top down onto the copper oxide surface)

to be defined to accommodate the large repeat unit were the bead-bead non-bond energy, the bead bond length (the repeat unit length was usually averaged from a larger molecular model of a polymer), the van der Waals (VdW) distance (usually derived from the molecular models when the non-bond energies are derived), and the bead bond force constant (derived from a molecular model in which a repeat unit stretched). In addition it was concluded that a last parameter was needed for realistic simulation of the stress-strain curve (to failure), which was not part of the Martini force field: a bead-bead bond length scission criterion. This criterion was found by stress-dynamic molecular models that stretched the repeat unit until bond distortion occurred so the atomistic bonds were ready to break, which was usually past the maximum in the energy to strain curves derived from the dynamics. The stress dynamics (using forcing potentials) were repeated at different speeds, and the maximum bead length determined at bond distortion (end-end distance) was plotted against the energy. It was found that the maximum bead length converged at a consistent length. This length was taken as the maximum that the bead will extend before scission occurs. The maximum bead bond length criterion was applied at every step in the mesoscale model, and bonds were deleted as soon as the criterion was met. It was found early on, while working on the simulations of adhesion and cohesion, that without it, the wrong interface was predicted to fail.

Figure 4.31 shows example energy trajectories of models used to determine the bead-bead non-bond energies. Figure 4.31a shows the cohesive case of the Delft epoxy, and Fig. 4.31b shows the adhesive case to copper oxide. For the cohesive case, it is almost always in the axial chain direction; for the adhesive case is it almost always parallel to the flat substrate surface (or if the substrate is another polymer, it ends up being similar to the cohesive case, in chain axial directions).

Coarse graining can be done in two ways within the Mesocite software package. The bead itself can be defined then the polymer built from each bead, or an initial network can be built in the molecular modeling builders, and the beads defined by the architecture defined in the molecular model. For these examples the latter was used and once the initial unit cell was built, supercells (replication of the initial unit cell) could be constructed to build the superstructure. Figure 4.32 shows some of the molecular models and their coarse-grained unit cells to illustrate the concept of the computational simplification possible with coarse graining. The cube at the far left

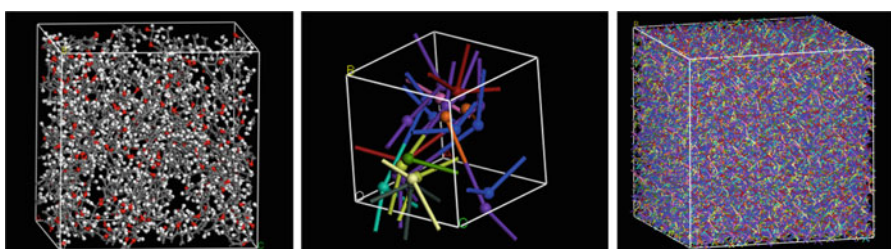


**Fig. 4.32** Left, molecular model (FW~23,000); middle, coarse-grained unit cell of molecular model (FW~23,000); right, optimized CG supercell (FW~8 M)

was the initial molecular model of the epoxy oligomer. The repeat unit (which consisted of the epoxy and curative) was used to define the coarse-grained “bead,” and the coarse-grained representative of the oligomer is shown by the middle cube of Fig. 4.32. Simplification of the model is demonstrated as the left and middle pictures represent the same molecular structure. The right cube represents the middle cube replicated until the total mass was well over 8 M. This initial coarse-grained model is 50 nm on a side, as shown in Fig. 4.32, far right. As current state-of-the-art IC features are now <10 nm, these coarse-grained models demonstrated that IC-size structures can be modeled explicitly; however, because of computational time constraints, the coarse-grained models were reduced to 12–15 nm structures. The coarse graining included the copper oxide-epoxy adhesive interface, in which the copper oxide was simply coarse-grained using its unit cell as the bead.

To create the copper oxide interface, a vacuum unit cell of the optimized supercells was created, which was then capped with a layer of copper oxide beads. The copper oxide beads were derived directly from a copper oxide crystalline unit cell. For simplicity (and in keeping with known experiment), it was assumed that the copper oxide did not fail. In this manner, the bonds of the copper oxide remained fixed, and just the non-bond interactions of the copper oxide-epoxy interface were parameterized, using the same procedures as before. An interface model of the copper oxide+epoxy was then constructed using a vacuum cell configuration (vacuum on either side of the copper oxide-epoxy bilayer) creating an infinite bilayer, and this interface construction was energy minimized. It was discovered that to obtain the highest interfacial energies, an additional compaction step was needed, in which the copper oxide was slowly moved down toward the epoxy and briefly equilibrated at room temperature at each step until a new constant energy optimum was found. Without the compaction step, the initially minimized interface was in a local, rather than a global minimum. In all cases the immediate bottom polymer beads next to vacuum were fixed to prohibit global movement of the layer and prevent unreasonable expansion of the polymer into the vacuum.

For the adhesion model, the copper oxide was stepwise displaced into the vacuum away from the polymer layer. Each displacement step was followed by a brief room temperature (RT) equilibration, in which the polymer was watched to see if it would follow the displacement of the interface due to the bond and non-bond interactions. In order to capture a non-equilibrium dynamic, each of the equilibration steps were kept to a minimum, just enough to get past the initially high energies imposed by the displacement step, but never enough to get to equilibrium. However the total number of RT equilibration steps was always kept constant, in order to approximate some relative level of “time.” In addition a second simulation was run to look at the pure cohesive interface. In this case, the same vacuum cell was used, but half of the polymer was stepwise displaced into the vacuum, each step also followed by a brief RT equilibration, again to see if the remaining epoxy would follow the rest of the mass. After each step for both the adhesive and cohesive cases, any bead bond that exceeded the maximum bond length criterion was severed. An example of starting and ending (after failure of the interface) models is shown in Fig. 4.33a, b. As with the molecular models, energy versus displacement curves could be

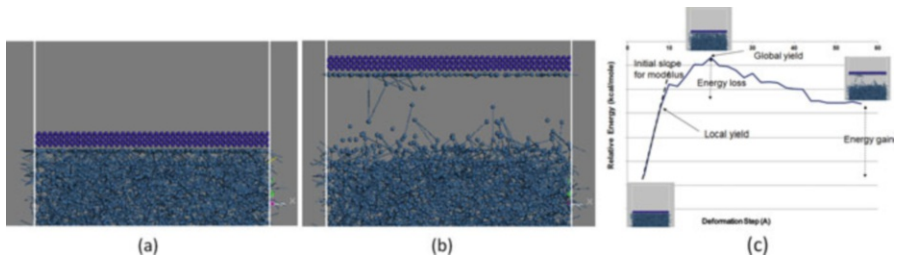


**Fig. 4.33** Before (a) and after (b) side views of the coarse-grained adhesive (vacuum cell) models, showing that failure occurs within the cohesive side of the interface (lighter colored polymer beads left on the darker copper oxide beads); (c) shows an example of the simulated stress-strain curve derived from the adhesion models represented in (a, b) and the associated properties that can be derived from the energy curve

constructed from which modulus, local yield (departure from elastic), global yield, energy gain (storage), and energy loss could be obtained. An example of such a curve is provided in Fig. 4.33c. Construction of these stress-strain curves from the mesoscale model energies has been previously covered in-depth [1, 59] so only the results of the analysis will be discussed here.

The best verification of using coarse-grained models came from two different areas of simulation. One was the modulus prediction based upon the cohesive simulations. It was found that the modulus predicted from the molecular models (2.0 GPa) was the same as the modulus predicted from the coarse-grained models (2.12 GPa) and both matched the experimental modulus ( $\sim$ 2.0 GPa), demonstrating a high degree of consistency across the length scales. The second example was the qualitative failure mode. Experimental test results indicated that adhesive failure occurred with some epoxy being left behind on the copper side. That is, failure was not pure adhesive failure that would have led to clean copper surfaces. The coarse-grained adhesive models demonstrated failure within the epoxy rather than clean adhesive failure. Both the modulus and the correct location of failure further demonstrated that a jump in coarse-grain scale to large grains could be done without loss in predictive power (and could be the start of even larger jumps, when software becomes available that will accommodate bead shapes). Start and end side views are shown in Fig. 4.33 of one of the adhesive cases. Clearly failure is in the polymer side of the interface; however, the failure is not purely cohesive either, as indicated in Fig. 4.34a, b. Here, the horizontal cut (rotated top-down view) of just the epoxy beads immediately next to the copper oxide layer at the start and at the end of the simulation is shown. As can be seen from the qualitative change in bead density of this layer, which decreases after failure, there is a mix of both adhesive and cohesive failure occurring, just like observed experimentally. The amount of material left behind after interfacial failure seems to track with the cross-link density and qualitatively tracks with the strength of the interface derived from the energetics. It is remarked that the competition between cohesive and adhesive failure by a continuum mechanics approach was discussed in Sect. 4.5 of the preceding chapter. Cross-

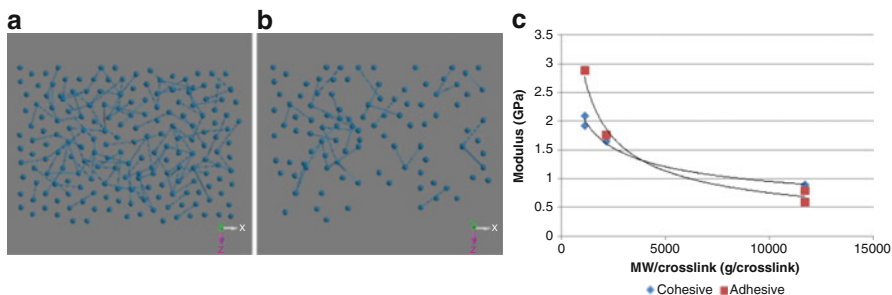


**Fig. 4.34** (a) Before and (b) after epoxy layer (top-down view) of the polymer layer immediately next to the copper oxide. The beads represent an epoxy repeat unit and the lines between them are the bead bonds; (c) impact of cross-link density on modulus

link density is another variable that was tracked in these models, and it was found that in general the modulus increases with cross-link density to a point (or decreases with the mass between cross-links) nonlinearly. Figure 4.34c shows the existence of a crossover point when the cross-link density is increased where the adhesive modulus starts to become significantly better than the cohesive modulus.

The base models were adjusted to include the effect of moisture content and interface roughness. An example of moisture impact on the adhesive model is shown in Fig. 4.35, which shows the side views of the start and end models. When compared to Fig. 4.33, it is obvious that the effect of moisture is to increase the amount of deformation before adhesive failure and also to decrease the amount of polymer left behind. That is, the models showed that the failure shifts toward adhesive interface failure. This should not be surprising because the models show that water tends to form its own layer on the copper oxide, which should disrupt some of the polymer adhesion to the substrate.

Roughness was another variable imparted to the adhesive interface by use of a sawtooth copper oxide interface. It was found that there is an angle dependence to the modulus trend, and the higher the sawtooth angle (which means a shallower sawtooth leading to lower shearing), the higher the adhesive modulus and the higher the energy gain of the system. Interestingly, something similar happens with the amount of material being left behind, with an increase in material at the higher sawtooth angle. This base trend is in keeping with the higher modulus but also agrees with the higher energy gain as more material is involved in the failure mechanism. There is an inflection found in all of these trends, suggesting the effect of roughness is nonlinear. Until now all of the adhesive models were run in the same deformation mode in which the copper oxide layer was moved in tension into the vacuum space of the unit cell. However it is possible to also move the copper oxide sideways, in order to investigate increasing shear. To investigate this mixed mode behavior, the flat adhesive interface models were moved in diagonal directions and compared to the sawtooth models which also should contain aspects of both shear and tension. Figure 4.36 shows that the modulus trends with deformation direction are nonlinear,

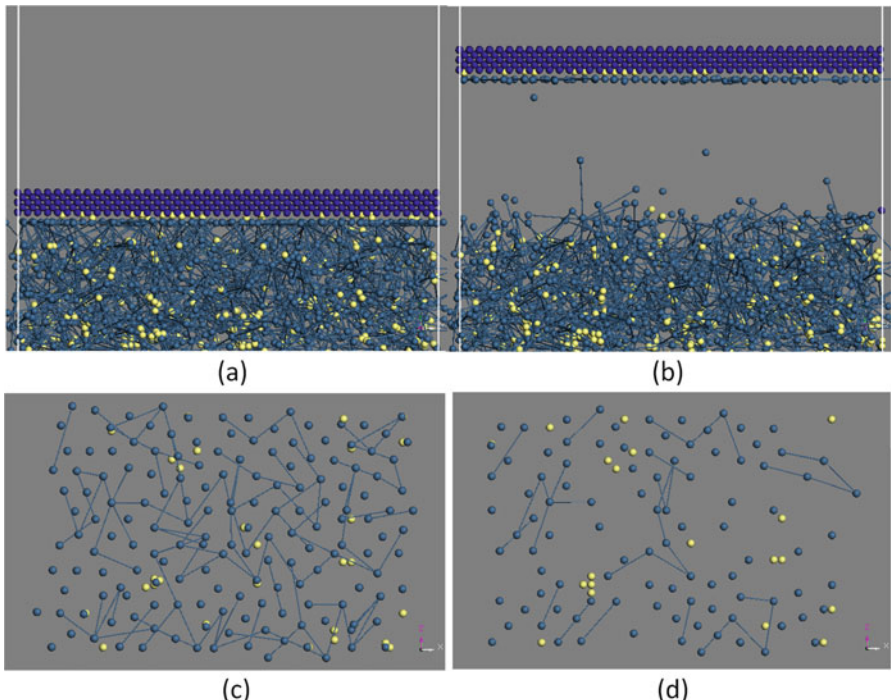


**Fig. 4.35** (a) Before and (b) after side view of the adhesive failure coarse-grained models with moisture involvement; (c) before and (b) after top down views of the polymer layer immediately next to the copper oxide with water beads involved (light-colored beads)

and the different model cases (flat vs. sawtooth) start to lay on top of one another. The shear direction is still showing the lowest modulus, and the tensile direction is showing the highest.

However the next case that was tried gave results that were totally unexpected. To test a mixed tension/shear case, one of the sawtooth cases was used and a sideways movement of the copper oxide across the sawtooth applied, as shown in Fig. 4.37. For this case the energy curves exhibited a cyclic response, as the epoxy polymers went under compression and tension with the sawtooth. The cycles were roughly equivalent to the period of the sawtooth, and the first cycle had an unusually high modulus (not expected from the trends in Fig. 4.36) that were much higher than those found in pure tension, which tapered off with cycling. In addition, at failure, when all bead bonds are broken, there was qualitatively much more material left behind than the original flat interface model, when Fig. 4.34a, b is compared to Fig. 4.37c which uses the same dimensional model, with only the roughness of the copper oxide changed. This suggested that the sawtooth does help to engage more material and lock-in more mass into the response.

Although these are not crystalline models, the observation that there may be material bunching or pileups depending upon the deformation and the roughness

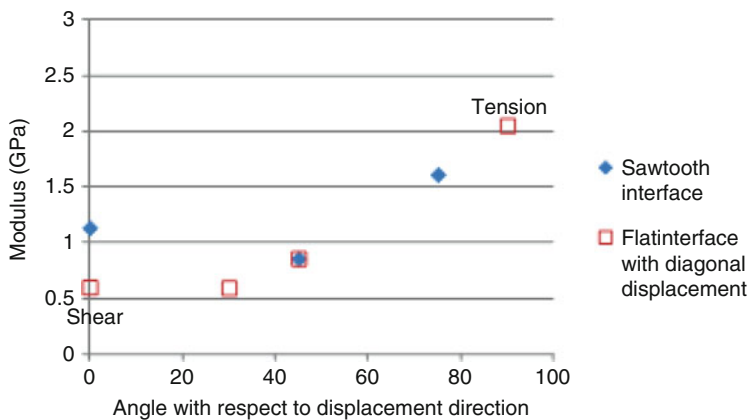


**Fig. 4.36** Angular dependence of displacement direction on the modulus

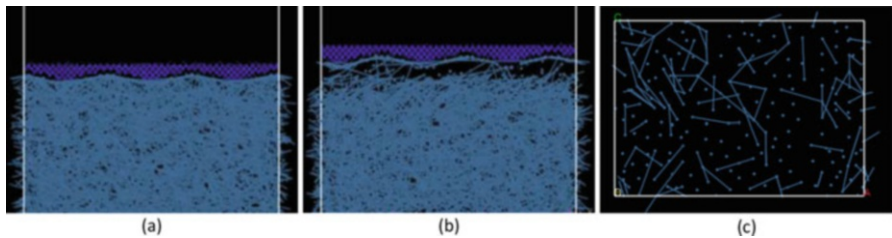


**Fig. 4.37** High sawtooth angle Cu<sub>2</sub>O interface in shear (horizontal direction), (a) at the start and (b) after failure; (c) polymer remaining on Cu<sub>2</sub>O side of interface at failure

brought up a similarity to grain-strengthening or the Hall-Petch relationship where dislocation pileups at grain boundaries increase strength [62]. In crystalline materials the Hall-Petch relationship shows that the yield is inversely proportional to the square root of the grain size,  $\sigma_y = \sigma_0 + kd^{-0.5}$ , where  $\sigma_y$  is the yield strength or hardness,  $d$  is the grain size, and  $\sigma_0$  and  $k$  are material constants. So if there is a similarity to the function of the sawtooth and grain size, a linear relationship should emerge if the inverse square of the yield strength is plotted against the sawtooth pitch to represent the grain size. When the global (maximum energy) and local (deviation from elastic) yields were extracted from the simulated stress-strain curves, it was found that the global yield energies do follow a Hall-Petch relationship with the sawtooth pitch (as do the energies extracted at maximum bond breakage, further tying the bond disruption to the yield). These findings have been reviewed previously [2], showing the Hall-Petch-like relationships found and the similarity to other strength concepts. For instance, maximizing the interactions to maximize the strength is not counter to polymer mechanistic concepts which optimize interactions that lead to limited kink movement. On a very basic molecular level, these mechanism all conceptually rely on maximizing physical interactions to maximize

deformation resistance (analogous the grain-strengthening argument). These interaction arguments are important to understand and develop, as they are the underlying basis of why molecular models can be used to engineer materials.

## 4.7 Mixed Modeling for Thick Film Dielectrics Used in Displays

This example shows aspects of different molecular models (DFT and MD) that were used in order to piece together the performance issues of a dielectric that was targeted for use in displays. There were two application areas of interest at the time: as a planarizing layer and as an encapsulating layer, shown in Fig. 4.38. Although not an IC packaging material, the application is involved in the packaging of light-emitting diodes (LEDs). Additionally the examples demonstrate that sometimes both classical and quantum techniques should be used to get the whole picture. More specifics have been previously reported [1, 2, 63–65].

### 4.7.1 Planarization Dielectric

During the development of this dielectric, which is an organo-silicate, significant shrinkage was found after cure (Fig. 4.39). The shrinkage was disconcerting because it was entirely unexpected based upon previous formulations. Reasons for the film shrinkage were thought to range from weight loss due to additional cure (and loss of silanol or alkoxy groups), weight loss due to depolymerization, or thickness loss due to packing or polymer rearrangement. Molecular modeling was engaged to determine which was more likely.

The first experimental data to be used for molecular modeling was that of an FTIR of the silicate layer. This would help piece together whether or not the polymer was

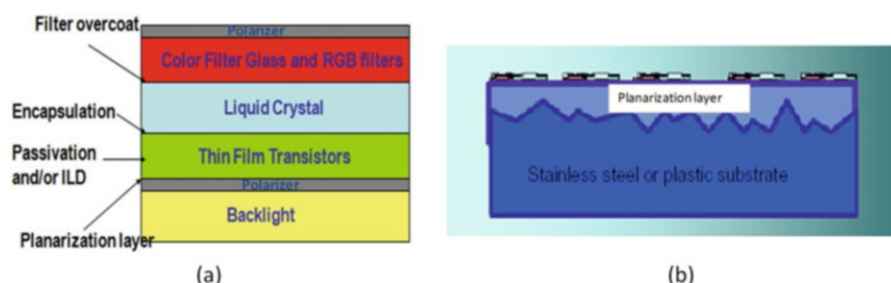


**Fig. 4.38** Use areas for thick film silicates. (a) General location of dielectrics (filter overcoats, transistor encapsulants, passivation layers, and planarization layers); (b) Schematic of use as a planarization layer

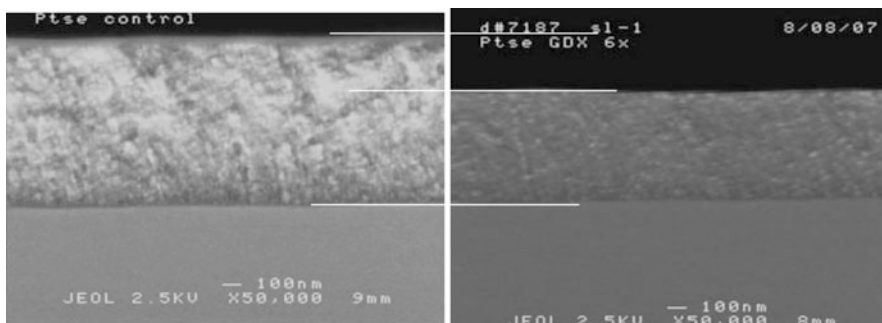


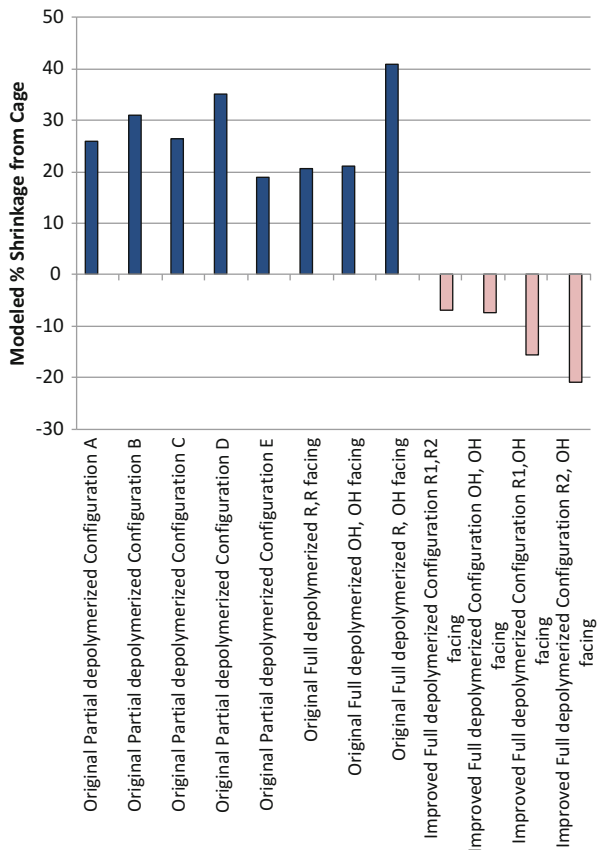
**Fig. 4.39** SEM cross section showing shrinkage of the silicate dielectric used as a planarization layer before cure (left) and after cure (right)

degrading. The FTIR results indicated that there was a significant loss in the cage content of the silicate architecture and an increase in the ladder content, which would indicate that additional cure was not causing shrinkage, but the architectures are devolving toward lower cure-type structures. While this alone would not support weight-loss theories from depolymerization, it did support the alternate theory of polymer rearrangement and compaction. It was also discovered that films with the most shrinkage were found contaminated with high levels of metals, but no weight loss differences could be found between the high metal formulations and low metal level formulations. This bolstered the theory that compaction could be a culprit due to known studies which found that metals could depolymerize silicates [66, 67]. If only partial depolymerization was occurring, then no weight loss would be observed, but the new oligomers might compact, which would explain the experimental findings.

The partial depolymerization and compaction were investigated in two ways. DFT was used to calculate the adsorption tendencies of the silicate for the metals, and reaction thermodynamics of cage depolymerization, and simple volume models of groups of silicate architectures (cages, ladders, and rings) were compared for the possible reaction products of cage depolymerization. In both cases, the depolymerized entities emerged as the likely culprit. From DFT, the metal centers were found to be energetically highly absorptive to the silicates, and opening of the cages to ladders and ring structures (the beginning of depolymerization for these structures) was thermodynamically highly exothermic and highly favorable. Partial rather than full depolymerization would explain the lack of weight loss repeatedly found in experimental testing done in parallel to the modeling efforts.

The volumes of simple pairs of depolymerized formulation component structures were then compared. These comparisons showed that up to 35–40% shrinkage (Fig. 4.40, dark bars) could occur upon full depolymerization of the cage structures, which is exactly what was observed. The same volume analysis was used to look at another proposed component (Fig. 4.40, light bars) which indicated there were compositions that might counter the shrinkage by offering some expansion. Formulation components were then looked at for the ability to resist the shrinkage forces

**Fig. 4.40** Simple pairwise volume changes of depolymerized cages. Captions show the state of polymerization in the model, as well as orientation of the R- and silanol groups (R1, R2, and OH)



that should exist during cure. This was done using forcing dynamics of formulation component pairs and testing for whether the expected interaction mechanics were enhanced or degraded. Figure 4.41 shows the results of this modeling test in which the moduli and relative strengths were simulated by forcing dynamics. According to these results, one of the newly proposed components should be better able to resist shrinkage. The formulation compositions were then computationally tested for volume change like before. One of the new formulations showed markedly improved shrinkage stability (which is contrasted to the original formulation in Fig. 4.41) and was chosen to move forward.

#### 4.7.2 Encapsulation Dielectric

Another application of a thick film silicate was as an encapsulation layer. The issue for this application was proximity to the liquid crystal (LC) within the display and the impact on the switching of the display pixels. It was thought that the dielectric

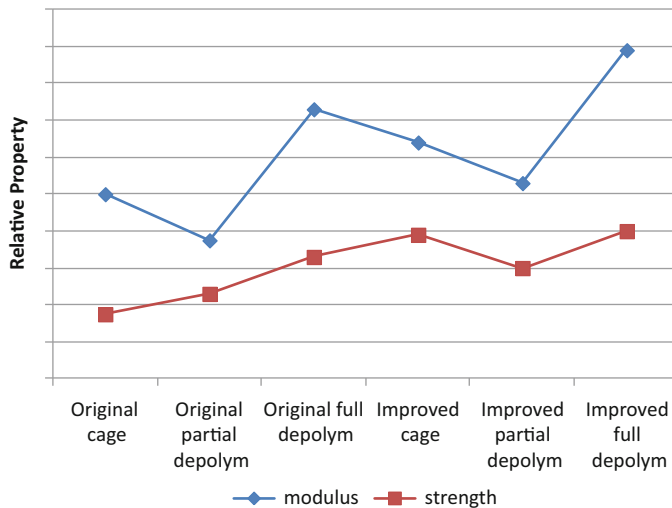
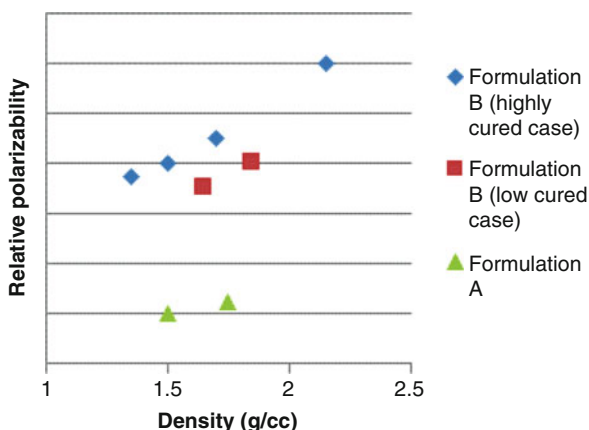


**Fig. 4.41** Results of modeling of improved formulation over the original showing general trend of improved modulus and strength when the new and original formulation is compared

could slow the switching speed of the IC by current leakage in the layer. To answer whether our dielectric could be involved, the band structures of the formulations were calculated by means of DFT. The bandgaps were estimated directly from conduction to valence bandgap in the band structure. It was found that the bandgaps could be manipulated and increased by choice of monomer and by adjusting the cure which would change the cured material structure, to further ensure that our materials were not causing leakage. In addition, the question was asked whether our material could be involved as part of the dielectric response due to the proximity next to the liquid crystal of the display. One standard test was the voltage holding ratio test (VHR) which tests the ability of a layer to hold a voltage. To answer this question, polarizabilities were calculated based on two of the leading formulations, representing different cure states (silanol content and density being two of the major variables). The higher polarizability was thought to be better for VHR, as it should be related to the ability to align with a field. The polarizabilities provided us with one of the best performance correlations, as one of the formulations (Formulation B in Fig. 4.42) showed consistently high values. This material also had higher measured dielectric constant, which is also consistent with its higher polarizability. When VHR testing was done at the customer, it was found that this same material was identified with the best VHR and these formulations were chosen for further development.

**Fig. 4.42** Calculated polarizabilities of test formulations



## 4.8 Coarse-Grained Diffusion in a Simulated Photoresist Polymer

Another application of coarse-grained models involved diffusion through a polymer [68]. Although the polymer was a simulated photoresist, this example is included because the main topic of diffusion is of general interest to packaging materials and further illustrates the usefulness of coarse graining. In this case, it was thought that one of the organic bases used in a layer next to the photoresist was poisoning the photoresist's acid catalyst so the question was posed to confirm that this was the case and coarse graining was used, encouraged by previous work looking at diffusion of fluorinated blowing agents [68]. The photoresist itself was approximated using methyl methacrylate in which the entire repeat unit was parameterized as a bead. The different bases simulated were based upon those known to be used in the layer next to the photoresist. They were generally highly hydrophilic molecules with an organic base head and a hydrophilic polymer tail. The beads were defined based upon the functionality of the base head and the repeat unit in the long chain tail. The different parameterizations that were constructed were based upon nine different interactions: base-base, base-tail, base-acrylate, base-water, tail-tail, tail-acrylate, tail-water, water-water, and water-acrylate. The bases were built using the same base head but varying the size of the tails to represent the sizes of bases available commercially.

A coarse-grained PMMA polymer mass was built and optimized (approximately  $200 \times 200 \times 350 \text{ \AA}$ ), and a  $200 \times 350 \text{ \AA}$  vacuum unit cell created with  $200 \text{ \AA}$  thickness. To force diffusion only in one direction, a physical barrier layer was also used consisting of a graphite layer placed near the top of the polymer mass. Usually molecular modelers do not use a barrier layer configuration for diffusion, but this proved to be a good practice in a past study in order to concentrate diffusion in one direction for the evaluation of fluorocarbon blowing agents [68].

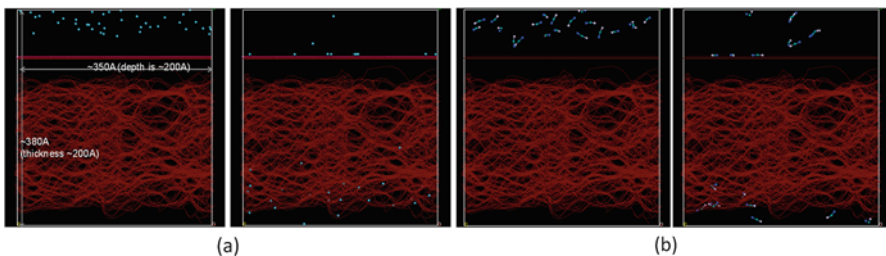


**Fig. 4.43** Example diffusions at the start (left) and end (right) of the simulations. **(a)** Small MW base diffusion; **(b)** larger MW

All of the interactions of the base components were parameterized using the same forcing potential technique previously used. However, because this was a diffusion model in which the average forward velocities during diffusion should be small, the non-bond energies were parameterized by the zero intercept of the energy-distance curves in order to establish a lower rate regime than that covered by the mechanical models. This is also the parameterization technique that was used previously for the blowing agents diffusion which found that by using non-bond forces more in-line with an unforced condition, realistic diffusion constants were found (both relative trends and extrapolated values). The barrier itself used artificially high non-bond interactions to prohibit diffusion through the layer (discovered by trial and error in the previous work on the blowing agents). The bases were applied in the vacuum space between the bottom of the polymer and the barrier layer and equilibrated at room temperature for 500 ps. This configuration would force diffusion only in one direction, but no forcing potential was used. In these examples, the direction is defined by where the diffusants are deposited relative to the barrier layer. Diffusion direction in these models is generally bottom to top of the unit cell. The barrier layer beads were fixed for all simulations. In addition, because of computer limitations, the polymer mass was fixed.

An example of before and after snapshots of the amine beads for a low MW and higher MW bases are shown in Fig. 4.43 with the polymer-barrier layer darkened more in order to highlight the light-colored bases. High penetration of the smallest base was found (Fig. 4.43a) which was parameterized as a single bead because of size. However, increasing the molecular weight (MW) started to prohibit penetration (Fig. 4.43b) indicating that MW is a major variable toward penetration into the polymer and may be a factor in the photoresist poisoning. The possibility of poisoning deep inside the photoresist layer is possible, if smaller bases are present.

In addition, moisture was applied within the bases (optimized together before applying them to the polymer) in the diffusion simulation. The trends were generally similar as those simulations without water, suggesting size is the predominant variable. Interestingly, water-induced agglomeration was found for the larger bases, which was expected due to the high hydrophilic nature of the tail used. Figure 4.44b shows an example of the base agglomeration due to water during the simulation. Agglomeration is very evident at the end where the bases have

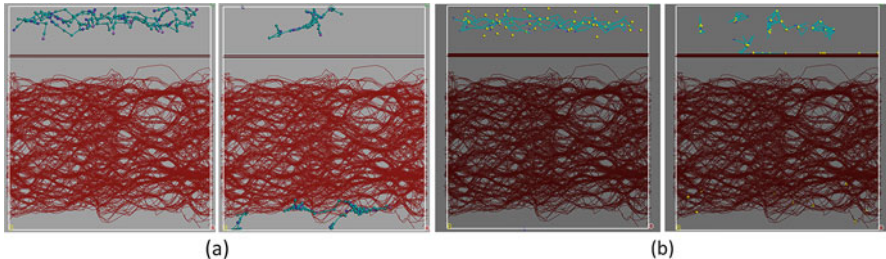


**Fig. 4.44** One of the largest bases simulated. The left side is the start of the simulation and the right side the end. **(a)** No water case showing no diffusion of the large base, but penetration into the acrylate (below) has begun; **(b)** case using moisture showing agglomeration of water with the base, which is highly hydrophilic showing even less movement of the base. The effective mass is larger, so there is no hint of penetration. Water is indicated by the light-colored isolated beads and the darker lines are the highly hydrophilic base, while the darkest lines are the acrylate polymer (below, as in **a**)

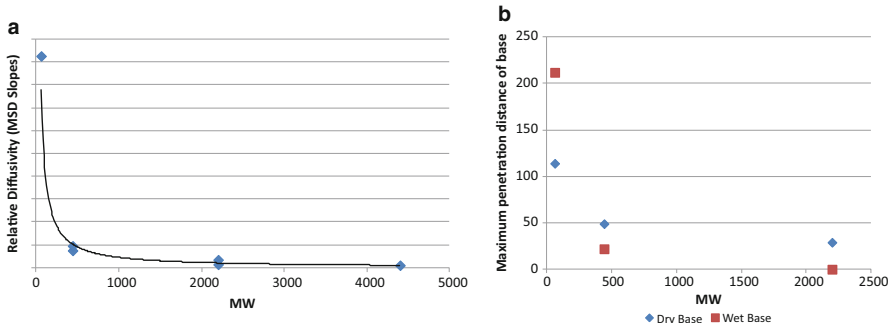


**Fig. 4.45** **(a)** Results of mean squared displacement (MSD) which estimates diffusivity; **(b)** maximum distance any base penetrated into polymer. Both show the MW dependency

agglomerated with water and with themselves. The effect can be compared to the case without water, which is shown in Fig. 4.44a in which the large base is just starting to penetrate the polymer. When agglomeration occurs, the artificially high mass (due to agglomeration) has not even approached close to the polymer, and only the small leftover water beads are beginning to penetrate further confirming the MW dependency of these bases.

Both the root-mean-squared displacements (MSD) and the maximum penetration (defined as the furthest distance a base unit diffused into the polymer) was measured and both confirmed that size was the major variable with and without moisture involved (Fig. 4.45). Remarkably, a small base, without the long hydrophilic tails of the other bases, has enhanced diffusion when moisture is involved, and maximum penetration occurs through the full thickness of the polymer layer. Testing has been limited but confirms that size for this type of organic base generally helps control diffusion as the simulations suggest.

Hydrophobic base examples have not yet been simulated, but the current simulations suggest we should see a different effect from lower hydrophilic bases. The surface diffusion trends of Sect. 4.4 suggest that a low hydrophilic nature should penetrate more given the lower surface energies of a hydrophobic material. That is, according to surface theory, lower surface energy liquids should have higher surface wetting, which should help penetrating power along the surfaces of the polymer strands. So extended wetting is expected into the material with the lower hydrophilic bases. We have seen evidence of this kind of penetration along polymers structures in other molecular modeling simulation studies of copper diffusion in porous dielectrics [12, 69, 70].

## 4.9 Atomistic Simulation of Porous Low-Dielectric Constant Materials

In this section, the chemical-mechanical relationship of the amorphous, porous silica-based low-dielectric (low-k) material (SiOC:H, also referred to as black diamond) is obtained by means of a series of atomistic simulations [71]. The molecular network structure is generated by means of given concentrations of four basic building blocks. This dielectric material was applied in IC backend structures of which the dielectric constant  $k$  can be reduced in two ways: (i) replacing oxygen by the methyl groups, H, or OH, or (ii) by creating porosity within the material [72]. The mechanical stiffness of this material is one of the main parameters that governs the reliability of IC backend structures. In order to understand the variation in the mechanical stiffness and density resulting from modifications to the chemical configuration, sensitivity analyses were performed. The trends indicated by the simulations exhibit good agreement with experimental data. In addition, the simulation result shows that Young's modulus of the SiOC:H is dominated by the concentration of only two basic building blocks, whereas the density is influenced by all the basic building blocks.

### 4.9.1 Atomistic Model of SiOC:H

A schematic picture of SiOC(H) is shown in Fig. 4.46 [73]. The different Si atoms are usually related to the number of linked O atoms: zero (Z), mono (M), di (D), tri (T), and quadri (Q). The bond terminators are of the type Si–R, where R is the –CH<sub>3</sub>, –O, and –OH functional group [74]. Measurement results [74] show that the concentration of Si–Si bonds is relatively low compared to Si–O and Si–C bonds.

Instead of generating the amorphous structure manually [75] or based on amorphous silicon [76], the SiOC:H structure is realized by means of the basic building blocks. The size of the void is assumed equal to the basic building blocks, while the groups are not allowed to connect to voids. It is further assumed that only a single

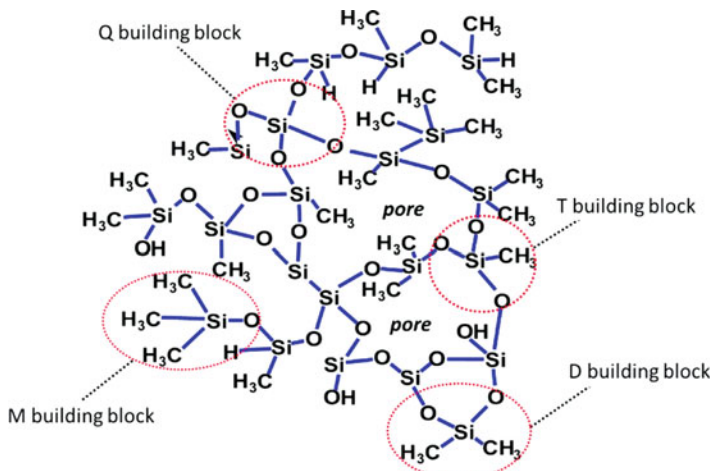


**Fig. 4.46** Chemical structure of SiOC:H illustrating the connection capability of the basic building blocks

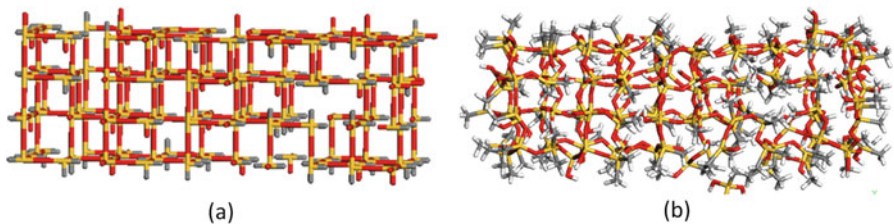


**Fig. 4.47** (a) Generated approximate molecular configuration of amorphous SiOC:H (b) is the molecule after minimization

bond exists between any two atoms. In order to establish the molecular model of SiOC:H, the concentration of the basic building blocks (from experimental data) is used as input to the algorithm. The distribution of the building blocks obeys three formulating rules, including the chemical characteristics of the Q, T, D, and M blocks, the average distribution of the basic building blocks, and the minimization of the dangling bond in the molecule. The stereochemical structure is established by minimizing the total potential energy of the aforementioned topology. Details of the algorithm are provided in [71]. An example of an approximate topology of SiOC:H is illustrated in Fig. 4.47. Due to the cubic framework, most of the atoms are not in a state of equilibrium. To minimize the potential energy, a structural relaxation, also known as the geometrical optimization procedure [77], is employed. Consequently, an approximate SiOC:H atomistic model is obtained; see Fig. 4.47b. This geometry is subsequently used as initial configuration in the MD simulations.

The accuracy of the thus obtained structure was qualitatively validated by considering two molecules: SiOC:H prior to and after UV treatment [71]. FTIR experiments [74] showed that the Si-O-Si bond angle is reduced after UV treatment. The results from the two models, based on the experimentally obtained building block concentrations, confirm the loss of the bond angles. In addition, the calculated Young's moduli and density values for materials show a good agreement with experimental values [78].

#### 4.9.2 Simulation Results

To study the effect of the separate building blocks on the resulting stiffness and density, a parametric study was performed in which several “series” were defined: series A is similar to the actual low-k materials, the chemical composition in series B is similar to A; the models C1, C2, and C3 emphasize the effect of Q, T, and D, respectively; and D1 is the extreme case air. The particular ratios are shown in Fig. 4.48a. The simulation results in terms of Young's modulus and density are given in Fig. 4.48b. Generally speaking, the A and B series show similar properties as the ratios of the different building blocks are comparable. For the C series, however, the simulated Young's moduli and densities exhibit large variation. Most prominently, the sensitivity shows that the basic building block Q positively affects Young's modulus and density while the amount of D appears to have an inverse effect on the properties. Clearly, increasing the porosity decreases both Young's modulus and density.

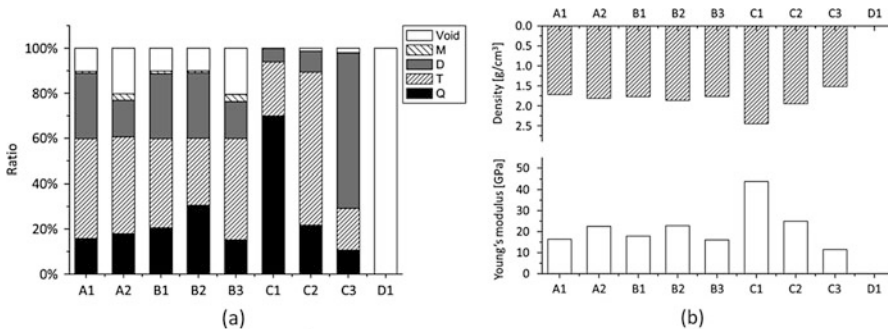


**Fig. 4.48** (a) Shows the ratio of building blocks for each model; (b) calculated Young's modulus and density values

## 4.10 Conclusions

This chapter attempted to underscore the versatility of molecular modeling to solve different issues that arise in the performance of materials and their interfaces used in electronics packaging. It concentrated on the use of comparison models in order to more quickly impact materials developed for specific applications, as well as on developing models that predict specific properties.

There have been many lessons learned and discovered over the course of doing materials development using molecular modeling, of which several are covered in this chapter: (1) Small forcing dynamic models are quick and give the right trends. (2) The impact of the substrate surface energy on wetting runs the opposite to the impact of the formulation on wetting. (3) The impact of moisture generally increases wetting (bleed) behavior above that predicted by theoretical trends alone, but which can be found directly in the simulation. It is most likely a combination of impacting the formulation surface energies and substrate. (4) Adhesion and cohesion trends are well-captured by the simple forcing dynamic model. The effect of moisture can be captured, and those interfaces more sensitive to plasticization by water can be found. (5) Stress-cycling simulations are better suited to understand reliability issues than a simple adhesion model (i.e., adhesion and cycling are not equivalent and must be used depending upon the performance requirement). (6) Moisture disruption of adhesion is demonstrated in the molecular models by the lower energies found. Energetically, water is found to weaken both the adhesive and cohesive side of the interface. (7) Scaling molecular models to larger models such as DEM can be done by providing key energy relationships from the molecular models. (8) Scaling molecular models to coarse-grained mesoscale models has been done with a jump in scaling using larger repeat units (rather than functional group) without degradation in predictive power which broadens the applicability of mesoscale models. (9) There is remarkable continuity between the elastic moduli found (molecular model, coarse grain, and experiment) suggesting a correlation between modulus and molecular level origins. (10) The coarse-grained mesoscale model also adequately reproduces the observed failure mode (mixed adhesive/cohesive failure), including the effects of water and interface roughness. (11) For the epoxy-copper oxide interface, mesoscale yield energies for the adhesive bond are found to be degraded more severely by moisture than the cohesive side, leading to the observed loss of adhesion. (12) Larger diffusion modeling can be accomplished using coarse-grained mesoscale diffusion in order to evaluate material trends, but care must be used in parameterizing the beads to reflect low global rates.

Due to the rapid development of micro-/nano-electronic technology, structures are approaching submicron and nanoscales. To design reliable structures and devices at low cost, it is essential to establish the structure-property relation, i.e., the relation that quantifies the critical properties (e.g., fracture toughness) as function of chemical composition, fabrication process, and dimension. Molecular modeling is advancing rapidly. With the advent of high-speed computing, larger molecular systems can be explicitly modeled. When combined with the advancements in

multi-scale methods, this results in truly predictive simulation capabilities at macroscopic (product) scale by means of dedicated scale bridging techniques, as discussed in Sect. 4.8 of the preceding chapter. Consequently, *materials and interface engineering* will become possible, most ideally within an industrial setting.

**Acknowledgments** The authors are grateful to the following colleagues, (former) students, and funding sources:

- Sections 4.3 and 4.6: Zhiwei Cui, Feng Gao, Stephen Todd, Gerard Goldbeck, as well as the partial financial support of the EC under contract NMP-2008-214371 NanoInterface (including providing of the software for the mesoscale simulations by Accelrys, Inc.) and the NSF grants (CMMI-1200075, CMMI 0726286)
- Sections 4.4, 4.5, 4.7, and 4.8: Charles Smith, Jess Pedigo, Alan Grieve, Shao Wei (Michelle) Li, Xiao-Qi (Charlie) Zhou, Masami Nakagawa (Colorado School of Mines), Graham Mustoe (Colorado School of Mines), Teri Baldwin, Joseph P. Kennedy, Brian Bedwell, Ahila Krishnamoorthy, Jelena Sepa, Ryan Hulse, Michael E. Thomas, and Ann Schoeb
- Section 4.9: Leo Ernst, Richard van Silfhout, Barend Thijssse, Francesca Iacopi, Amy Flower

## References

1. Iwamoto N, Yuen M, Fan H (2012) Molecular modeling and multiscaling issues for electronic material applications, vol 1. Springer Science Business Media LLC. Springer, <https://www.springer.com/us/book/9781461417279>
2. Wymyslowski A, Iwamoto N, Yuen M, Fan H (2015) Molecular modeling and multiscaling issues for electronic material applications, vol 2. Springer Science Business Media LLC. Springer, <https://www.springer.com/us/book/9783319128610>
3. Iwamoto N (2000) Advancing materials using interfacial process and reliability simulations on the molecular Level. In: 5th international symposium and exhibition on advanced packaging materials, Braselton
4. Bicerano J (1996) Prediction of polymer properties, 2nd edn. Marcel Dekker, New York
5. Koch W, Holthausen M (2001) A chemist's guide to density functional theory, 2nd edn. Wiley-VCH Verlag GmbH, Weinheim
6. Dauber-Osguthorpe P, Roberts V, Osguthorpe D, Wolff J, Genest M, Hagler A (1988) Structure and energetics of ligand-binding to proteins – escherichia-coli dihydrofolate reductase trimethoprim, a drug-receptor system. Protein Struct Funct Bioinforma 4:31–47
7. Sun H (1994) Force field for computation of conformational energies, structures, and vibrational frequencies of aromatic polyesters. J Comput Chem 15:752–768
8. Buehler M (2008) Atomistic modeling of materials failure. Springer Science+Business Media, LLC
9. Iwamoto N, Moro L, Bedwell B, Apen P (2002) Understanding modulus trends in ultra low k dielectric materials through the use of molecular modeling. In: The 52nd electronic components and technology conference, San Diego
10. Iwamoto N, Baldwin T (2014) Uncovering the origins of subtle solvation-based film defects. In: IEEE international conference on thermal, mechanical and multi-physics simulation and experiments in microelectronics and Microsystems, Ghent

11. Iwamoto N, Kennedy J, Varaprasad D, Mukhopadhyay S (2016) Understanding process cycling in thin film dielectrics. In: IEEE international conference on thermal, mechanical and multi-physics simulation and experiments in microelectronics and Microsystems, Montpellier
12. Thomas M, Iwamoto N, Smith D, Wallace S (2002) Transport phenomenon in porous low-k dielectrics. In: Semiconductor international
13. Ercolessi F (1997) A molecular dynamics primer, spring college in computational physics. ICTP, Trieste
14. Rapaport D (2004) The art of molecular dynamics simulation. Cambridge University Press, Cambridge
15. Ciccotti G, Hoover W (1986) Molecular-dynamics simulation of statistical-mechanical systems. Elsevier Science & Technology. Elsevier
16. Jones J (1924) On the determination of molecular fields. II. From the equation of state of a gas. Proc R Soc Lond Ser 106:463–477
17. Morse P (1929) Diatomic molecules according to the wave mechanics. II. Vibrational levels. Phys Rev 34:57–64
18. Stillinger F, Weber T (1985) Computer simulation of local order in condensed phases of silicon. Phys Rev B 31:5262–5271
19. Tersoff J (1986) New empirical model for the structural properties of silicon. Phys Rev Lett 56:632–635
20. Haile J (1992) Molecular dynamics simulation. Wiley, New York
21. Sadeghinia M, Jansen K, Ernst L (2012) Characterization and modeling the thermo-mechanical cure-dependent properties of epoxy molding compound. Int J Adhes Adhes 32:82–88
22. Schulz M, Frisch H (1994) Monte Carlo studies of interpenetrating polymer network formation. J Chem Phys 101:10008
23. Fan H, Yuen M (2007) Material properties of the cross-linked epoxy resin compound predicted by molecular dynamics simulation. Polymer 47:2174–2178
24. Mijovic J, Zhang H (2004) Molecular dynamics simulation study of motions and interactions of water in a polymer network. J Phys Chem B 108:2557–2563
25. Yarovsky I, Evans E (2002) Computer simulation of structure and properties of crosslinked polymers: application to epoxy resins. Polymer 43:963–969
26. Wu C, Xu W (2006) Atomistic molecular modelling of crosslinked epoxy resin. Polymer 47:6004–6009
27. Varshney V, Patnaik S, Roy A, Farmer B (2008) A molecular dynamics study of epoxy-based networks: cross-linking procedure and prediction of molecular and material properties. Macromolecules 41:6837–6842
28. Lin P, Khare R (2010) Local chain dynamics and dynamic heterogeneity in cross-linked epoxy in the vicinity of glass transition. Macromolecules 43:6505–6510
29. Ford D, Tack J (2008) Thermodynamic and mechanical properties of epoxy resin DGEBA crosslinked with DETDA by molecular dynamics. J Mol Graph Model 26:1269–1275
30. Li C, Strachan A (2011) Molecular dynamics predictions of thermal and mechanical properties of thermoset polymer EPON862/DETDA. Polymer 52:2920–2928
31. Fan H, Chan E, Wong C, Yuen M (2006) Investigation of moisture diffusion in electronic packages by molecular dynamics simulation. J Adhes Sci Technol 20:1937–1947
32. Kacar G, Peters E, de With G (2015) Multi-scale simulations for predicting material properties of a cross-linked polymer. Comput Mater Sci 102:68–77
33. Kacar G, Peters E, van der Ven L, de With G (2015) Hierarchical multi-scale simulations of adhesion at polymer–metal interfaces: dry and wet conditions. Phys Chem Chem Phys 17:8935–8944
34. Yang S, Qu J (2012) Computing thermomechanical properties of crosslinked epoxy by molecular dynamics simulations. Polymer 53:4806–4817
35. Bandyopadhyay A, Valavala P, Clancy T, Wise K, Odegard G (2011) Molecular modeling of crosslinked epoxy polymers: the effect of crosslink density on thermomechanical properties. Polymer 52:2445–2452

36. Marrink S, de Vries A, Mark A (2004) Coarse grained model for semiquantitative lipid simulations. *J Phys Chem B* 108:750–760
37. Shinoda W, Devane R, Klein M (2007) Multi-property fitting and parameterization of a coarse grained model for aqueous surfactants. *Mol Simul* 33:27–36
38. Yang S, Cui Z, Qu J (2014) A coarse-grained model for epoxy molding compound. *J Phys Chem B* 118:1660–1669
39. Lorenz C, Stevens M, Wool R (2004) Fracture behavior of triglyceride-based adhesives. *J Polym Sci B Polym Phys* 42:3333–3343
40. Yang S, Qu J (2014) Coarse-grained molecular dynamics simulations of the tensile behavior of a thermosetting polymer. *Phys Rev E* 90:012601
41. Li J (2003) AtomEye: an efficient atomistic configuration viewer. *Model Simul Mater Sci Eng* 11:173
42. Stevens M (2001) Interfacial fracture between highly cross-linked polymer networks and a solid surface: effect of interfacial bond density. *Macromolecules* 34:2710–2718
43. Yang S, Qu J (2014) An investigation of the tensile deformation and failure of an epoxy/Cu interface using coarse-grained molecular dynamics simulations. *Model Simul Mater Sci Eng* 22:065011
44. Delle Site L, Abrams C, Alavi A, Kremer K (2002) Polymers near metal surfaces: selective adsorption and global conformations. *Phys Rev Lett* 89:156103
45. Yang S, Gao F, Qu J (2013) A molecular dynamics study of tensile strength between a highly-crosslinked epoxy molding compound and a copper substrate. *Polymer* 54:5064–5074
46. Fish J (2006) Bridging the scales in nano engineering and science. *J Nanopart Res* 8:577–594
47. Geers M, Kouznetsova V, Matouš K, Yvonnet J (2016) Homogenization methods and multiscale modeling: non-linear problems. In: Encyclopedia of computational mechanics, 2nd edn. Wiley, p TBD. Wiley: <https://doi.org/10.1002/9781119176817.ecm2107>
48. Iwamoto N, Pedigo J, Grieve A, Li M (1998) Molecular modeling as a tool for adhesive performance understanding. In: Proceedings of the MRS 98 symposium J: electronic packaging materials science X. San Francisco
49. Iwamoto N, Pedigo J (1998) Property trend analysis and simulations of adhesive formulation effects in the microelectronics packaging industry using molecular modeling. In: Proceedings of the 48th electronic components and technology conference, Seattle
50. Iwamoto N (1999) Simulating stress reliability using molecular modeling methodologies. In: 32nd international symposium on microelectronics, Chicago
51. Iwamoto N (2000) Advancing polymer process understanding in package and board applications through molecular modeling. In: Proceedings of the 50th electronic components and technology conference, Las Vegas
52. Pedigo J, Iwamoto N, Zhou C (2000) Via-fill materials for next generation interconnect. *HDI Mag* 3:36–45
53. Cooper W, Nuttall W (1915) The theory of wetting, and the determination of the wetting power of dipping and spraying fluids containing a soap basis. *J Agric Sci* 7:219–239
54. Goldmann L, Howard R, Jeannotte D (1997) Package reliability. In: Microelectronics packaging handbook. Springer, pp 405–555. Springer: <https://www.springer.com/us/book/9780412084317>
55. Iwamoto N, Li M, McCaffrey S, Nakagawa M, Mustoe G (1998) Molecular dynamics and discrete element modeling studies of underfill. *Int J Microcircuits Electron Packag* 21:322–328
56. Iwamoto N, Nakagawa M (2000) Molecular modeling and discrete element modeling applied to the microelectronics packaging industry. In: Micro materials 2000 conference, Berlin
57. Mustoe G, Nakagawa M, Lin X, Iwamoto N (1999) Simulation of particle compaction for conductive adhesives using discrete element modeling. In: Proceedings of the 49th electronic components and technology conference, San Diego
58. Bossis G, Brady J (1984) Dynamic simulation of sheared suspensions. I. General method. *J Chem Phys* 80:5141

59. Iwamoto N (2012) Developing the stress-strain curve to failure using mesoscale models parameterized from molecular models. *Microelectron Reliab* 52:1291–1299
60. Iwamoto N (2013) Molecularly derived mesoscale modeling of an epoxy/Cu interface: interface roughness. *Microelectron Reliab* 58:1101–1110
61. Stewart J, Marrink S, Risselada H, Yefimov S, Tielman D, de Vries A (2007) The MARTINI force field: coarse grained model for biomolecular simulations. *J Phys Chem B* 111:7812–7824
62. Nieh T, Wadsworth J (1991) Hall-petch relation in nanocrystalline solids. *Scr Metall Mater* 25:955–958
63. Iwamoto N, Krishnamoorthy A, Spear R (2009) Performance properties in thick film silicate dielectric layers using molecular modeling. *Microelectron Reliab* 49:877–883
64. Iwamoto N, Krishnamoorthy A (2009) Understanding leakage current susceptibility in dielectrics using molecular modeling. In: 10th international conference on thermal, mechanical and multi-physics simulation and experiments in microelectronics and microsystems (EuroSimE), Delft
65. Rutter E, Krishnamoorthy A, Iwamoto N (2010) Novel organosiloxane polymers with improved device properties. In: 14th meeting of the symposium on polymers for microelectronics, Wilmington
66. Okamoto M, Suzuki S, Suzuki E (2004) Polysiloxane depolymerization with dimethyl carbonate using alkali metal halide catalysts. *Appl Catal A Gen* 261:239–245
67. Okamoto M, Miyazaki K, Kado A, Suzuki E (2001) Deoligomerization of siloxanes with dimethyl carbonate over solid-base catalysts. *Chem Commun* 18:1838–1839
68. Hulse R, Bogdan M, Iwamoto N (2011) Predictive model for polyurethane blowing agent emission into a house. In: Polyurethane conference, Nashville
69. Iwamoto N, Thomas M (2003) Simulating diffusion through porous materials using molecular modeling. In: International conference on metallurgical coatings and thin films, San Diego
70. Iwamoto N (2004) Molecular modeling studies of IC barrier concerns. In: Proceedings of the 5th international conference on thermal and mechanical simulation and experiments in microelectronics and microsystems (EuroSimE), Brussels
71. Yuan C, van der Sluis O, Zhang G, Ernst L, van Driel W, van Silfhout R, Thijssse B (2008) Chemical-mechanical relationship of amorphous/porous low-dielectric film materials. *Comput Mater Sci* 42:606–613
72. Maex K, Baklanov M, Shamiryan D, Lacopi F, Brongersma S, Yanovitskaya Z (2003) Low dielectric constant materials for microelectronics. *J Appl Phys* 93:8793–8841
73. Yuan C, van der Sluis O, Zhang G, Ernst L, van Driel W, Flower A, van Silfhout R (2008) Molecular simulation strategy for mechanical modeling of amorphous/porous low-dielectric constant materials. *Appl Phys Lett* 92:061909
74. Iacopi F, Travaly Y, Eyckens B, Waldried C, Abell T, Guyer E, Gage D, Dauskardt R, Sajavaara T, Houthoofd K, Grobet P, Jacobs P, Maex K (2006) Short-ranged structural rearrangement and enhancement of mechanical properties of organosilicate glasses induced by ultraviolet radiation. *J Appl Phys* 99:053511
75. Gaskell P, Tarrant I (1980) Refinement of a random network model for vitreous silicon dioxide. *Philos Mag Part B* 42:265–286
76. Guttmann L, Rahman S (1988) Simulation of the structure of amorphous silicon dioxide. *Phys Rev B* 37:2657–2668
77. Accelrys (2005) Materials studio-discover. Accelrys Inc., San Diego
78. Yuan C, van der Sluis O, Zhang G, Ernst L, van Driel W, van Silfhout R (2007) Molecular simulation on the material/interfacial strength of the low-dielectric materials. *Microelectron Reliab* 47:1483–1491